Mon. Not. R. Astron. Soc. **269,** 67–88 (1994)

The scatter-broadened image of Cygnus X-3

P. N. Wilkinson,[1] R. Narayan[2] and R. E. Spencer[1]

[1] *University of Manchester, Nuffield Radio Astronomy Laboratories, Jodrell Bank, Macclesfield, Cheshire SK11 9DL*
[2] *Harvard-Smithsonian Center for Astrophysics, Harvard University, 60 Garden Street, Cambridge, MA 02138, USA*

Accepted 1994 January 31. Received 1994 January 31; in original form 1993 December 8

ABSTRACT

We have made observations of the highly scatter-broadened image of Cygnus X-3, using MERLIN at both 408 and 1692 MHz. At each frequency the shape of the image is close to that of an elliptical Gaussian, but the ellipticity and the position angle are frequency-dependent. We interpret the variable elongation of the scattering disc as being due to scale-dependent anisotropy in the scattering medium arising from variations in the direction of the projected interstellar magnetic field. From the scale on which the anisotropy changes we derive a value for the outer scale of turbulent density fluctuations, $r_{\rm out} \sim$ few $\times 10^{11}$ km ~ 0.01 pc. Cyg X-3 is the third source for which the scattering disc has been shown to be markedly elliptical for at least one wavelength. This suggests that anisotropy in the turbulent ISM may be a widespread phenomenon, and emphasizes the importance of extending scattering theory to include its effects on observations.

At both frequencies our interferometer data show an excess of correlated flux density at large baselines compared with that expected from a pure Gaussian image profile. This excess visibility power is due to weak image granulation and was predicted for a power-law spectrum of turbulence by Goodman & Narayan. From the amplitude of the excess visibility power we constrain the exponent in the power-law spectrum to be < 3.83. This is consistent with several other indications for a 'shallow' spectrum, i.e. an exponent below 4. In the rest of the analysis we have assumed an exponent of 11/3, which corresponds to a Kolmogorov spectrum.

We employ three different methods to estimate the inner scale $r_{\rm in}$ of the density power spectrum in the scattering screen in front of Cyg X-3: (i) from the wavelength-dependence of scatter-broadening; (ii) from the visibility as a function of those baselines where the source is moderately resolved; and (iii) from the excess power in the visibility on baselines where the source is highly resolved. From a combination of the results from methods (ii) and (iii) we cautiously constrain $r_{\rm in}$ for this line of sight to lie in the range $10^2 < r_{\rm in} < 10^{5.5}$ km.

Future MERLIN and VLBI measurements should be able to place better constraints on the spectrum of density fluctuations, using the analysis methods we present here. However, in view of the subtlety of the effects being sought, obtaining data of the requisite quality will always present a significant observational challenge.

Key words: plasmas – radiative transfer – turbulence – techniques: interferometric – ISM: magnetic fields – ISM: structure.

1 INTRODUCTION

The only way to study the small-scale density fluctuations in the ionized component of the interstellar medium (ISM) is to observe their effect on the propagation of radio waves (e.g. Rickett 1977, 1990; Narayan 1988, 1992). Studies of the angular and temporal broadening due to scattering are possible for pulsars, while angular broadening and image wander measurements can be made for extragalactic radio sources. The evidence suggests that turbulence in the ISM has a smooth component, uniformly distributed throughout the Galaxy (Cordes, Weisberg & Boriakoff 1985) plus, at low

galactic latitudes, regions of greatly enhanced scattering. These may be associated with supernova remnants (Gwinn, Bartel & Cordes 1993) or H II regions (Anantharamaiah & Narayan 1988; Fey, Spangler & Cordes 1991).

The understanding of scattering by the ISM and its effect on the complex visibility function measured by a radio interferometer has progressed significantly in recent years (Cohen & Cronyn 1974; Romani, Narayan & Blandford 1986; Goodman & Narayan 1989, hereafter GN89; Rickett 1990; Narayan & Goodman 1989). This theoretical work has focused observers' attention on the possiblity of measuring the shape of the spatial frequency spectrum of density fluctuations and the inner and outer scales of turbulence by using interferometric data. These properties can, in principle, be inferred from measurements of the first-order effects of angular and temporal broadening and their variation with wavelength. Furthermore, higher order effects, for example image granularity (GN89), should also be observable depending on the shape of the spectrum of turbulence. Unfortunately, not only are these effects subtle and therefore hard to observe, so are the wavelength-dependent changes in the first-order effects. This places a great premium on obtaining high-quality measurements of the interferometer visibility function, spanning a large range of baselines at several wavelengths, if the phenomenology of turbulence in the ISM is to be understood.

Cyg X-3 is a highly variable radio source at a distance of at least 10 kpc (Dickey 1983, adopting a Galactic Centre distance of 8.5 kpc) which is situated behind a region of the Galactic plane associated with unusually large scattering (Fey, Spangler & Mutel 1989). The scattering towards Cyg X-3 (~ 0.45 arcsec at 1 GHz, Anderson et al. 1972; Wilkinson, Spencer & Nelson 1988) is exceeded by only three other lines of sight through the Galaxy: towards NGC 6334B (~ 7 arcsec at 1 GHz, Moran et al. 1990), towards the Galactic Centre (~ 1.4 arcsec at 1 GHz, Davies, Walsh & Booth 1976), and towards 1849+005 (~ 1.1 arcsec at 1 GHz, Fey et al. 1991). Cyg X-3 is particularly well-suited for detailed studies of scattering. First, it has occasional outbursts when its flux density reaches many Jy at centimetre and decimetre wavelengths, and hence observations with very high signal-to-noise ratio (SNR) are possible. Secondly, if one observes within a few days of the peak of an outburst, the effects of intrinsic source structure can be ignored at decimetre wavelengths; the diameter of the scattered image is many times larger than the intrinsic source size calculated from the expansion rate of ~ 10 mas per day (Spencer et al. 1986; Molnar, Reid & Grindlay 1988; Schalinski et al. 1993a).

In this paper, we describe results from observations made with MERLIN (Thomasson 1986) at 408 MHz, during an outburst in 1986 January, and at 1692 MHz during an outburst in 1989 June. These data are currently the best of their type and enable us to investigate in some detail the properties of the turbulent ISM in a direction of greatly enhanced scattering. In Section 2, we describe the observations and the initial data analysis, which reveals that the scattered image of Cyg X-3 is more elongated at 1692 MHz than at 408 MHz and that the position angles of the two images are different. In Section 3, we discuss the varying ellipticity and suggest that it is due to anisotropy in the scattering screen associated with magnetic fields changing direction on scales smaller than the scattering disc at 408 MHz. We use our measurements of the disc size to derive an estimate of the outer scale of turbulence. In Section 4, we discuss the limits that our data place on the inner scale of turbulence and suggest ways in which the constraints can be strengthened. Finally, in Section 5, we briefly compare our results with results for other strongly scattered lines of sight through the Galaxy.

2 OBSERVATIONS AND INITIAL DATA ANALYSIS

2.1 The 408-MHz data

The 408-MHz data were taken with MERLIN from 1900 UT on 1986 January 3 to 1200 UT on 1986 January 4. While the results of a preliminary analysis of these observations were reported by Wilkinson et al. (1988), we now present a considerably more detailed study of the same data. At the time of these observations, MERLIN operated with six telescopes providing baselines ranging from ~ 6 to ~ 135 km; the 76-m diameter Lovell telescope at Jodrell Bank was used as the home-station telescope. January 3 was about 4 days after the peak of the burst seen at 2695 MHz (Johnston et al., in preparation), but the multifrequency observations of the 1972 burst (Hjellming 1989, and references therein) showed that at frequencies well below 1 GHz the peak comes later and is flatter-topped than at 2695 MHz. Our analysis was not significantly affected by variations in the total flux density during the 17-h run.

The visibility data were coherently averaged to 320 s, and the amplitude scale was calibrated by observations of unresolved sources before and after the run; we made no attempt to calibrate the visibility phases by observations of nearby point sources. The thermal noise on baselines involving the Lovell telescope ($1\sigma \sim 11$ mJy in 320 s) was about three times better than on the other baselines. Unfortunately, due to a problem with the correlator, the data from one of the most useful of the 15 baselines (between the Lovell and the Knockin telescopes, length ~ 60 km) were corrupted and had to be discarded. The u, v coverage of the data set, including the effects of further editing as discussed below, is shown in Fig. 1.

Fig. 2 shows the correlated flux density data plotted as a function of baseline length. The flux densities fall off monotonically with increasing baseline from a zero baseline value of 3.10 Jy. They exhibit very little dispersion from a smooth downward trend, and this immediately shows that the image is not split up into significant subcomponents nor is it highly elliptical. On baselines longer than ~ 60 km, less than half the length of the maximum projected baseline, the amplitude falls below ~ 75 mJy, i.e. $\sim 7\sigma$ on the Lovell baselines and $\sim 2\sigma$ on the other baselines. There remains, however, significant power on the longer baselines. Particularly on baselines involving the Lovell telescope, low-level (10–20 mJy) signals can be discerned out to the longest baseline of 127 km. The presence of this power at high spatial frequencies, at or below ~ 1 per cent of the power at zero spatial frequency, shows that there is weak substructure in the image.

We tried first to make an image of the source using conventional hybrid-mapping techniques (e.g. Cornwell & Wilkinson 1981), but this failed to produce a satisfactory

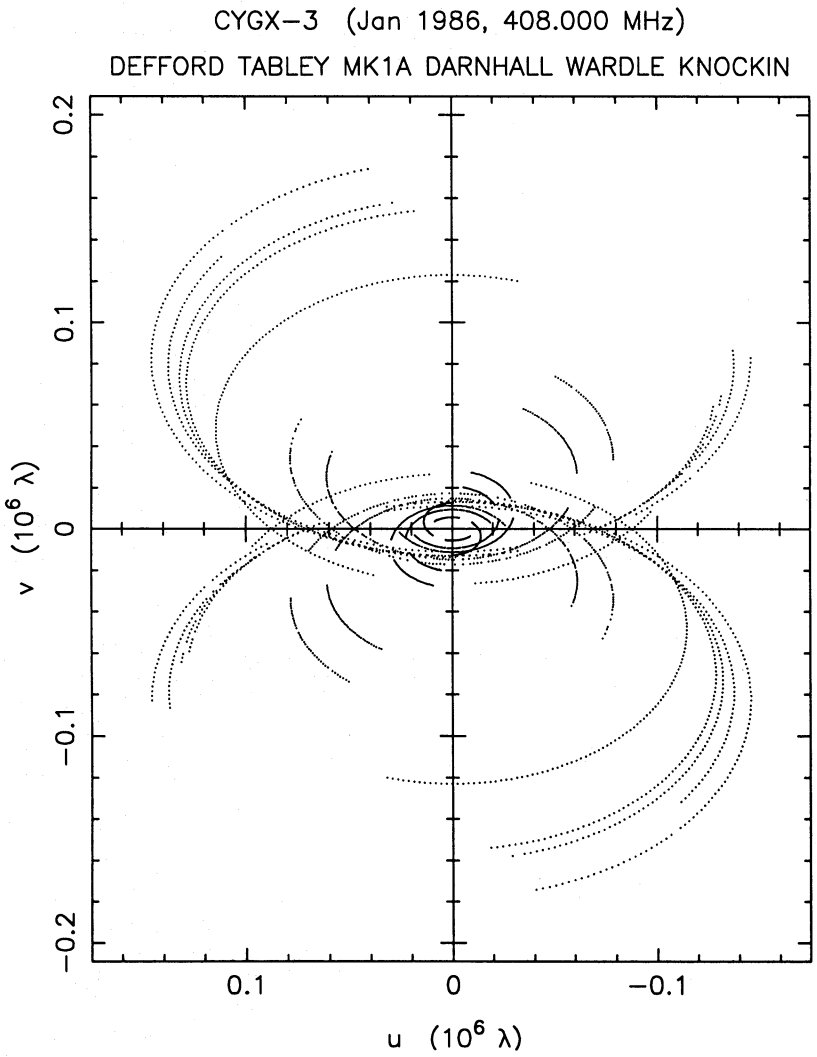

Figure 1. The u, v coverage at 408 MHz.

result. By making a series of tests with simulated data, which had closely similar SNR and u, v coverage to the actual data set, we confirmed that a circular Gaussian source of this size (FWHM ~ 3 arcsec at 408 MHz, i.e. three times larger than the MERLIN resolution) could not be properly reconstructed from our data set. One of the reasons is that most of the low SNR data on the longer baselines are not very useful for self-calibration. However, even if the visibility phases had been perfectly known, the image fidelity would not have been high. To make an image of a large Gaussian-like source, using a method that makes no strong assumptions about the form of the brightness distribution, requires a better-filled aperture plane than MERLIN was able to provide at that time.

We therefore analysed the data by model-fitting, and in several other ways which we will discuss in Section 4. Because we are looking for subtle effects in this data set, we deleted data from four of the short baselines that are affected by nearby confusing sources, leaving a total of 10 baselines for the remainder of the analysis. We also deleted much of the lowest SNR data. The presence or absence of signal can most simply be determined by examining the visibility phases after self-calibration; the reduced phase scatter when the SNR is greater than unity is readily discernible by eye. We retained data only where the visibility phase showed that the SNR was $\gtrsim 1{:}1$.

The simplest way to characterize the structure is to model-fit assuming that the source is an elliptical Gaussian. Since we know that the source structure is determined entirely by interstellar scattering, and since the substructure in the image is very weak, this is a good assumption. The shape of the scattering disc resembles rather closely that of an elliptical Gaussian, slightly elongated (axial ratio 0.88) along position angle (p.a.) 3°. The parameters of the best-fitting Gaussian model are listed in Table 1.

2.2 The 1692-MHz data

The 1692-MHz data were taken with MERLIN from 22 UT on 1989 June 3 to 23 UT on 1989 June 4, beginning about a day after the peak of a rather short burst (Johnston et al., in preparation). At this time one of the 18-m elements of the Cambridge 'One Mile Telescope' was incorporated into MERLIN, thereby increasing the maximum baseline length

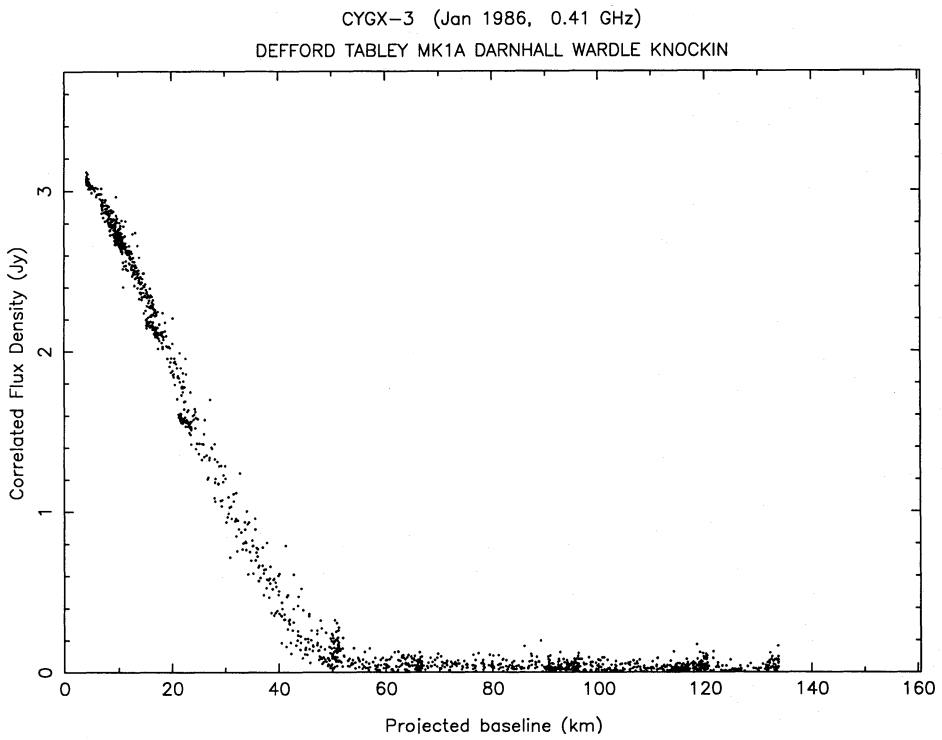

Figure 2. The correlated flux densities at 408 MHz plotted as a function of baseline length in km. The error bars have been omitted for clarity; the thermal noise levels are discussed in Section 2.1.

Table 1. Parameters of the elliptical Gaussian models fitted to the 408- and 1692-MHz data.

Frequency (MHz)	Flux Density (Jy)	Major Axis (arcsec)	Minor Axis (arcsec)	Axial Ratio	P.A. (°)
408	3.06	3.10 ± 0.05	2.73 ± 0.05	0.88 ± 0.02	3 ± 2
1692	5.10	0.172 ± 0.004	0.130 ± 0.003	0.76 ± 0.02	62 ± 1

to ~217 km and improving the u, v coverage. The Lovell telescope was again used as the home-station element. The data were coherently averaged for 10 min, and the resulting 1σ thermal noise levels ranged from ~2 mJy on many of the Lovell baselines to ~17 mJy on the least sensitive, Cambridge–Defford, baselines. Nevertheless, because the peak flux density (5.10 Jy) was higher and the source was less resolved than at 408 MHz, the SNR for all the 1692-MHz data is high. Although of good quality, the data from the shortest (~6 km) baseline were affected by confusion from nearby sources and were not used in the subsequent analysis. The u, v coverage for the final 1692-MHz data set is shown in Fig. 3.

Fig. 4 shows the correlated flux density data at 1692 MHz, plotted as a function of baseline length. The upper and lower envelopes fall off smoothly from the zero-baseline value of 5.10 Jy but, in contrast to the situation at 408 MHz, the amplitudes at any given baseline length have a marked dispersion. This immediately shows that the source is significantly elongated. An elliptical Gaussian model whose major axis lies along p.a. 62° and whose axial ratio is 0.76 provides an excellent fit to the data on all but the longest baselines. The parameters of this model are given in Table 1.

Since the scattered image is relatively compact and the SNR on all baselines was good, we were able to make a hybrid map of the source using the Caltech VLBI software package (Pearson 1991). The effect of a slight decay in the overall flux density during the run was corrected by amplitude self-calibration. Because the source size is comparable with the conventional restoring beam (~0.15 arcsec), a CLEAN image of the source does not show the details of the image at all well. We therefore deconvolved the final image using the maximum-entropy task VTESS in the NRAO AIPS package. The statistical entropy constraint, favouring smooth images, is a priori well-suited for this particular deconvolution problem. The VTESS image is shown in Fig. 5. The image resembles rather closely that of an elliptical Gaussian, although the logarithmic contouring scheme required to represent the large range of brightnesses with a reasonable number of contours tends to exaggerate the deviations from a simple ellipticity in the outer regions of the image: note that the outermost contour corresponds to only one-thousandth of the peak brightness.

In order to quantify the deviations from Gaussian symmetry, we used the AIPS task IMFIT to find the elliptical Gaussian that best fits this image. The parameters of this Gaussian were consistent with those determined by model-fitting directly to the visibility data and listed in Table 1. We then subtracted this Gaussian from the VTESS image; the residual image is shown in Fig. 6. The peak brightness in this image is only 3.4 per cent of the peak brightness in Fig. 5,

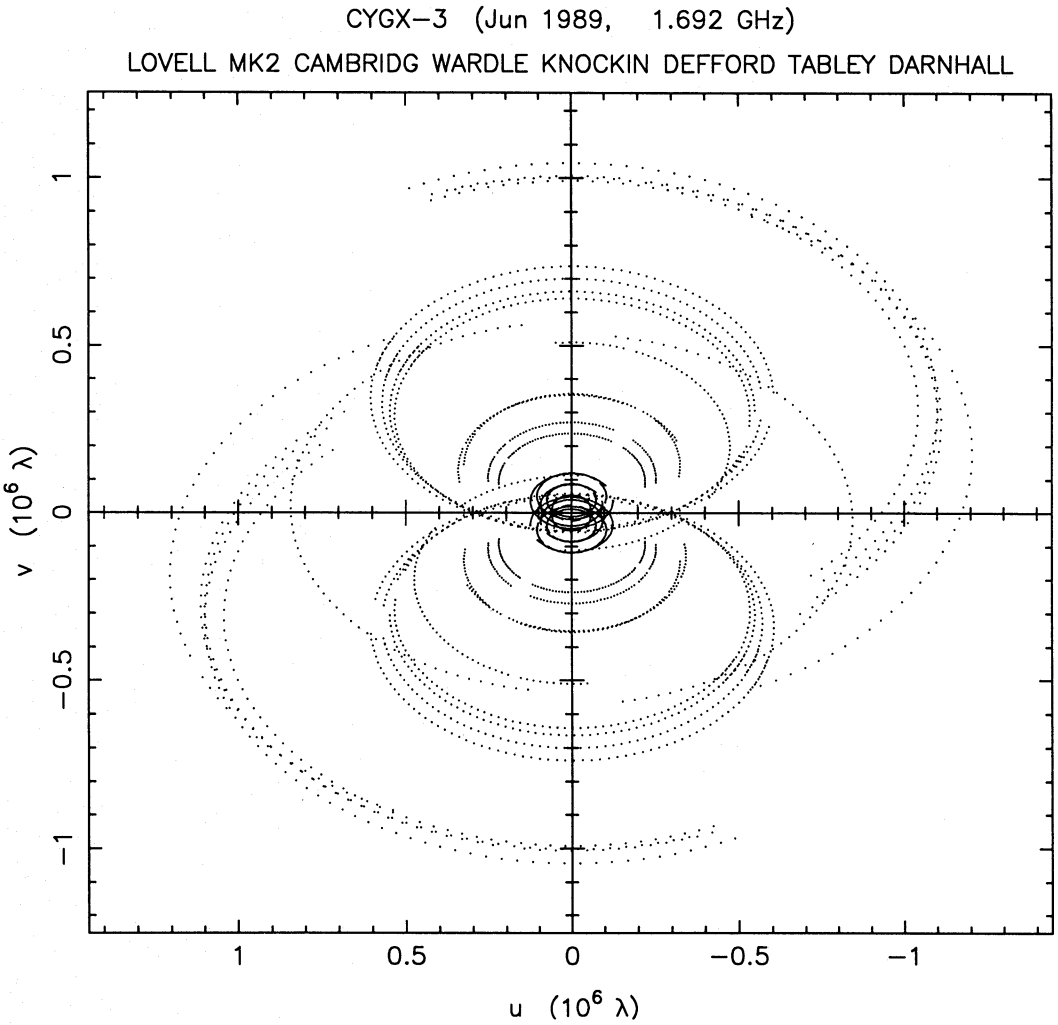

Figure 3. The u, v coverage at 1692 MHz.

confirming that the deviations from elliptical Gaussian symmetry are small.

3 INTERPRETATION OF IMAGE ELONGATION

3.1 Anisotropy in the scattering medium

To our knowledge, Cyg X-3 is the third case of a radio image displaying the effects of anisotropic scattering in the ISM. Spangler & Cordes (1988) showed that the brightness distribution of 2013+370 at 1.663 GHz is close to that of an elliptical Gaussian with an axial ratio of 0.70. Lo et al. (1993) showed that the scattered image of the radio source at the Galactic Centre at 8.4 GHz has an axial ratio of 0.49 ± 0.06. For Cyg X-3 we find an axial ratio of 0.76 ± 0.02 at 1692 MHz, and of 0.88 ± 0.02 at 408 MHz.

Before going on to discuss our preferred interpretation of our Cyg X-3 results, it is important to note that random elongations in the image can occur as a consequence of 'refractive effects' associated with density fluctuations on scales comparable to the projected image. To quantify the effect on the image, Romani et al. (1986) introduced an image anisotropy parameter e_s,

$$e_s = \frac{2(\theta_{max} - \theta_{min})}{(\theta_{max} + \theta_{min})}, \quad (1)$$

where θ_{max} and θ_{min} are the angular diameters of the image along the major and minor axis, respectively. Assuming a Kolmogorov spectrum of turbulence, they derived an estimate for the rms value of e_s. To make use of this estimate we have to anticipate results presented later in the paper, and we must also modify the estimate for the case when the inner scale of turbulence r_{in} is larger than the diffraction scale (see Section 4.1.1). We obtain, approximately,

$$(e_s)_{rms} \sim \left(\frac{r_{in}}{\theta_{mean} D}\right)^{1/6}, \quad (2)$$

where $\theta_{mean} D$ is the mean angular diameter of the image projected on the scattering screen. Taking θ_{mean} to be the geometric mean of the major and minor axes of the Gaussians listed in Table 1, and assuming $D \sim 2$ kpc (Fey et

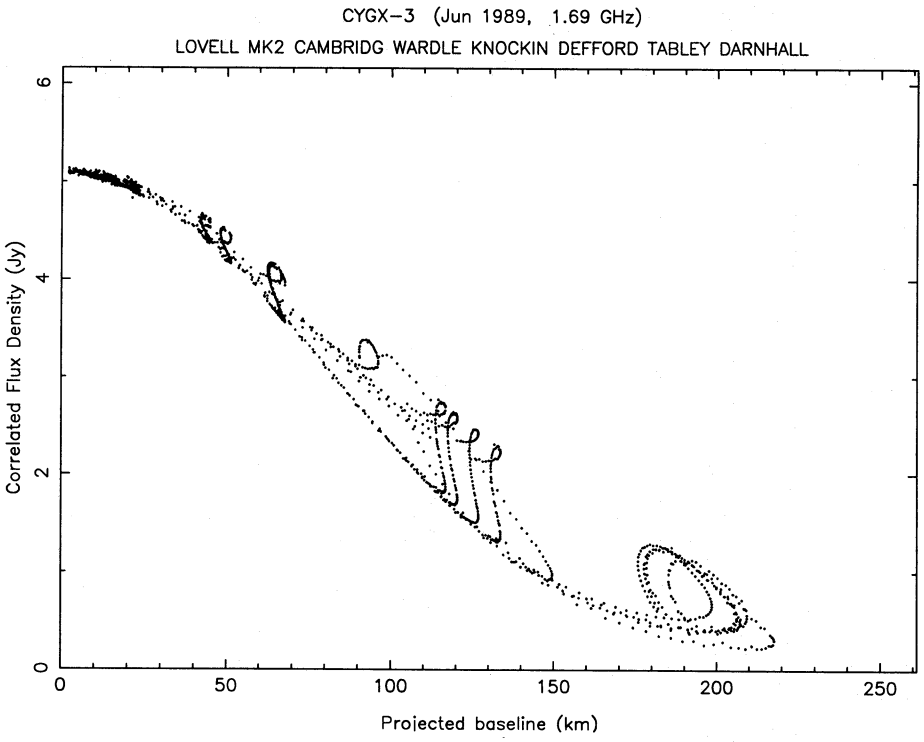

Figure 4. The correlated flux densities at 1692 MHz plotted as a function of baseline length in km. The error bars have been omitted for clarity; the thermal noise levels are discussed in Section 2.2.

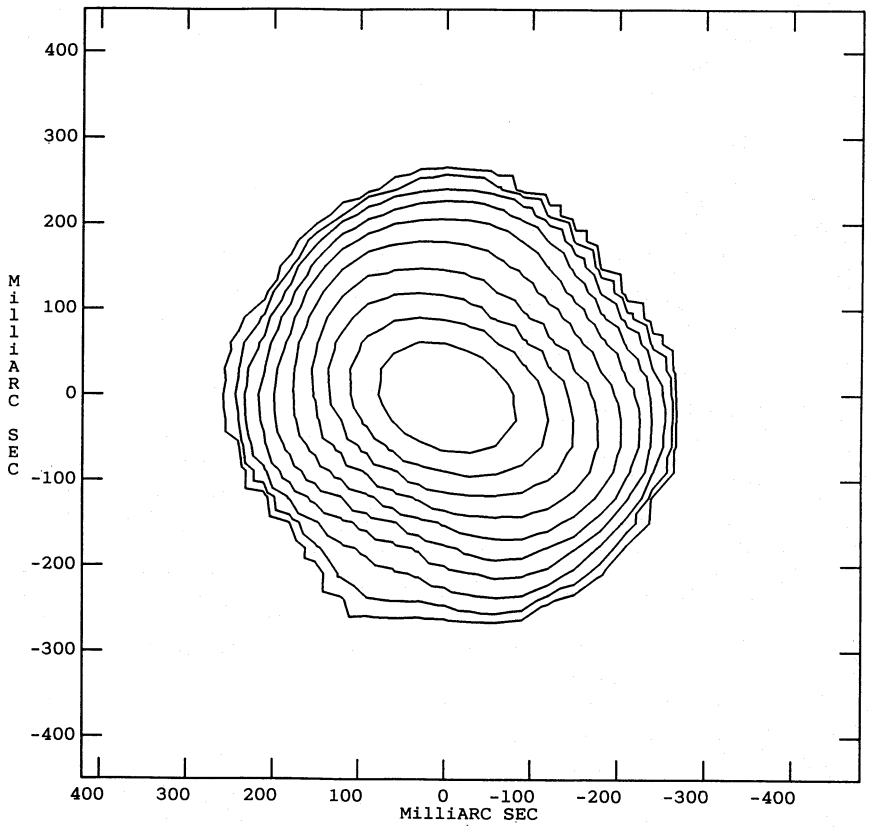

Figure 5. The VTESS (maximum-entropy) image of Cyg X-3 at 1692 MHz. The contour levels are 0.1, 0.2, 0.4,…, 51.2 per cent of the peak brightness of 0.181 Jy per pixel (pixel size 0.030 arcsec).

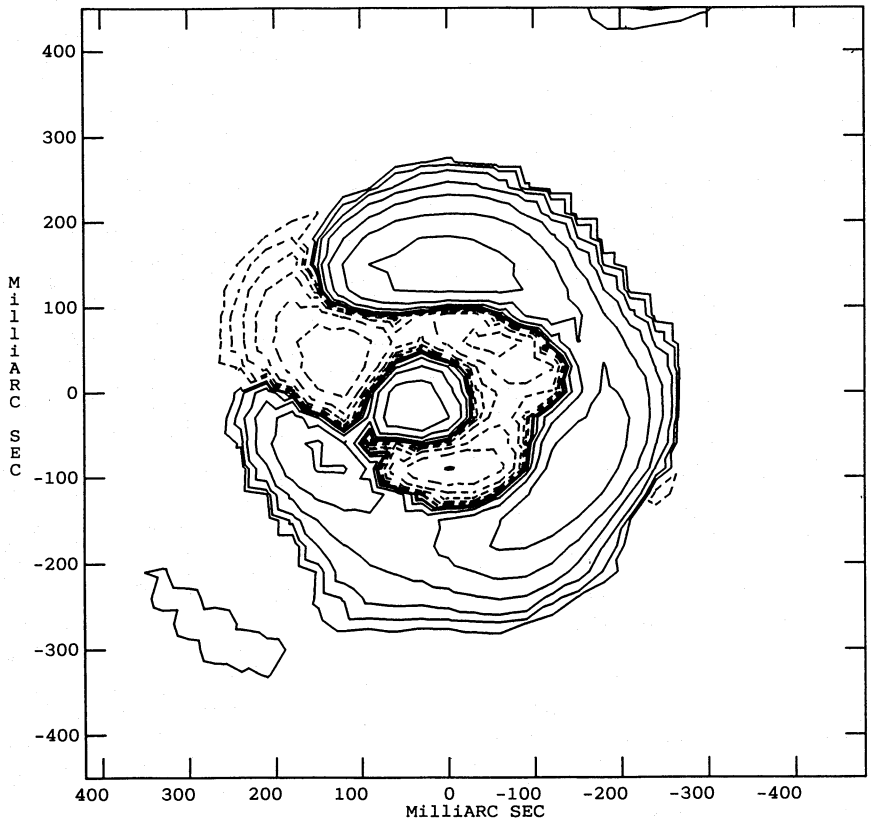

Figure 6. The residual image at 1692 MHz after the best-fitting Gaussian has been subtracted from the image shown in Fig. 5. The peak brightness in the map is 6.22×10^{-3} Jy per pixel, i.e. 3.4 per cent of the peak brightness in Fig. 5. The contour levels are -25.6, -12.8, -6.4, -3.2, -1.6, -0.8, -0.4, 0.4, 0.8, 1.6, 3.2, 6.4, 12.8, 25.6×10^{-4} Jy per pixel.

al. 1991), we find

$$(e_s)_{\mathrm{rms},408} \sim 0.07(r_{\mathrm{in}}/10^5 \text{ km})^{1/6},$$

$$(e_s)_{\mathrm{rms},1692} \sim 0.11(r_{\mathrm{in}}/10^5 \text{ km})^{1/6}. \quad (3)$$

From Table 1, the actually observed image anisotropy parameters are $(e_s)_{408} = 0.13$ and $(e_s)_{1692} = 0.28$. These are significantly larger than the rms value expected, even for the largest inner scales that we can allow ($10^{5.5}$ km, see the discussion in Section 4). We therefore feel that it is unlikely that the observed image elongations could be produced merely by random fluctuations in the scattering medium. We are further influenced by the fact that much more extreme anisotropy has been seen in another source ($e_s = 0.68$ for the source at the Galactic Centre, and such large axial ratios cannot possibly be produced by random fluctuations if the power-law spectrum of turbulence is 'shallow', i.e. the exponent is less than four (see the discussion in Section 4.1.1).

The obvious interpretation of the elongations is that they arise from striations in the scattering medium aligned perpendicularly to the major axis of the image – the striations scattering more effectively transverse to their long axis. In the case of Cyg X-3, the 1692-MHz image in Fig. 5 implies that these striations are oriented along p.a. $-28°$. However, we then have to explain the surprising difference between the images at 408 and 1692 MHz, in both the ellipticity (0.88 and 0.76, respectively) and p.a. (3° and 62°).

One way to account for the difference between the two images is to suppose that the scattering medium changed during the 42 months between the two observations, but we can discount this possibility on both theoretical and observational grounds. First, projected on the scattering screen, the 408-MHz image corresponds to a linear size of $4.4 \times 10^{11}(D/1 \text{ kpc})$, where we take the distance to the scattering screen to be D. Assuming $D \sim 2$ kpc, this means that the screen would have had to move with a velocity $\sim 10^4$ km s^{-1} in order to have brought a fresh region of the screen in to the line of sight during the time between the two observations. Such a velocity is unreasonably large. Secondly, an elliptical Gaussian model fitted to MERLIN data taken at 1.66 GHz in 1986 October, when the source was in quiescent mode (flux density 0.056 Jy), has a major axis of 0.165 arcsec, a minor axis of 0.145 arcsec, and a p.a. of 63°. The differences between these parameters and those determined from the 1989 June data are not significant, given the moderate SNR of the 1986 October data. This is direct evidence that the scattering screen did not change significantly over a period of three years.

We must also consider whether the 408-MHz image, being elongated north–south and therefore close to the intrinsic angle of ejection (Spencer et al. 1986), could be significantly affected by emission left over from a previous outburst. Strom, van Paradijs & van der Klis (1989) have mapped faint emission symmetrically disposed about the central compact

source and aligned approximately north–south. Its angular extent in 1987 October, ~6 arcsec, is consistent with expansion at ~0.010 arcsec per day (the same as the initial expansion rate) from the time of the 1985 December–1986 January outburst. We observed on 1986 January 4, about three months after a previous outburst, but the e-folding time for the decay of an outburst at 408 MHz is about a week (e.g. Hjellming 1989) and the quiescent flux density at decimetric wavelengths is less than 100 mJy (Nelson 1989). In addition, the angular extent of the ejecta associated with the 1985 October outburst at the time of our observations must have been ~0.9 arcsec – a factor of 3 smaller than the FWHM of the scattering disc we observed. Overall, we think it unlikely that 'relict' emission had a significant effect on our 408-MHz image.

The explanation that we consider most reasonable for the differences in the ellipticity and orientation between the 408- and 1692-MHz images is that we are resolving the correlation scale of the striations in the scattering screen. As mentioned above, the 408-MHz image has a projected size of $4.4\times10^{11}(D/1\ \mathrm{kpc})$ km, while the 1692-MHz image has a size of only $2.3\times10^{10}(D/1\ \mathrm{kpc})$ km. We propose that the striations in the scattering screen change direction on a scale ~few $\times10^{11}$ km. Because of the weaker scattering at 1692 MHz, the scatter-broadened image at this frequency samples a coherent patch of the medium and therefore displays the full anisotropy. VLBI observations of Cyg X-3 at 5 GHz (Schalinski et al. 1994) show several components of the intrinsic source structure, and it is noteworthy that these components have the same ellipticity and orientation as our 1692-MHz image, implying that their shape is governed by scattering. This result is consistent with our picture, since at 5 GHz the source is much smaller than the 1692-MHz image – hence the components sample the same coherent patch. On the other hand, at 408 MHz, the image is larger than the coherence scale of the striations, and so the observed image corresponds to an average over several independent patches. The averaging leads to a decrease in the degree of ellipticity compared to the 1692-MHz image, and also to a different image orientation. We expect that at yet lower frequencies the image will be even more circular than at 408 MHz.

3.2 Magnetic fields and the outer scale of turbulence

How do these striations arise? We believe that they are a magnetic effect. Much larger levels of ellipticity ($>5{:}1$) have been seen in scattering by the solar wind close to the limb of the Sun (Cornwell, Anantharamaiah & Narayan 1989; Narayan, Anantharamaiah & Cornwell 1989; Armstrong et al. 1990). In these observations the scattered image of the radio source 3C 279 had its long axis nearly tangentially oriented with respect to the solar limb, and it was natural to interpret the anisotropy as arising from a magnetic effect. Magnetic field lines in the solar corona are combed parallel to the radial direction by the outward motion of the solar wind. Turbulent density fluctuations in this ordered magnetic field will then naturally set up rod-like structures aligned with the field (cf. Higdon 1984, 1986; Goldreich & Sridhar 1994). This causes the scattered image of the source to appear elongated perpendicular to the radius vector to the Sun.

Theoretical models of the density fluctuations that produce interstellar scattering are usually based on ideas from magnetohydrodynamic turbulence (e.g. Higdon 1984, 1986; Goldreich & Sridhar 1994). In such models the velocity and density perturbations in the medium are intimately tied to magnetic field fluctuations. In particular, the coherence scale of the large-scale magnetic field is usually considered to be the same as the *outer scale* of the turbulence r_{out}, the lengthscale on which energy is fed into the turbulent cascade. On this assumption we conclude that, for the dominant scattering zone in the line of sight to Cyg X-3, r_{out} ~few $\times10^{11}$ km ~0.01 pc. This is probably the first direct measurement of the outer scale of the turbulence in any region of the ISM.

We can now ask what determines the actual degree of ellipticity observed in the scattered image at 1692 MHz. According to our model, this image samples a single coherent patch of the projected field, so that there is no reduction of anisotropy due to any transverse averaging (as there is at 408 MHz). Further, as we describe later, the scattering that we observe is predominantly due to density fluctuations on scales much smaller than the outer scale (for a 'shallow' spectrum, see Sections 3.3 and 4.1.1), and the MHD turbulence models clearly predict that such small-scale scattering blobs should be highly anisotropic (Higdon 1984, 1986; Goldreich & Sridhar 1994). Why then is the 1692-MHz image not much more anisotropic? We believe that we are seeing the effect of averaging along the line of sight. We suggest that the primary scattering screen towards Cyg X-3 is ~few $\times10^{12}$ km thick, so that it extends over several field coherence scales. This introduces a certain amount of averaging, leading to the modest axis ratio of 0.76 in the observed image at 1692 MHz. The line-of-sight averaging will, of course, be independent of frequency, and so we predict the same axis ratio of 0.76 at all frequencies above ~1 GHz, as seems to be confirmed by the 5-GHz data of Schalinsky et al. (1993b). Note that in the case of the solar wind the field coherence scale is likely to be essentially equal to the thickness of the scattering screen, and so much larger anisotropy can be observed (Narayan et al. 1989).

3.3 Parameters of the scattering screen

Our model of the scattering layer in front of Cyg X-3 involves two apparent coincidences. First, we require the thickness of the screen to be comparable to the outer scale. This is probably not so unusual, since in most models of turbulence the outer scale does tend to be similar to the overall size of the medium. The second coincidence is of more concern; namely, that the outer scale happens to lie conveniently between the two lengthscales probed by our two scatter-broadened images.

Accepting our model of the scattering screen towards Cyg X-3, however, we can use our estimates of the screen thickness and outer scale to derive estimates of other physical quantities in this screen. If the rms fluctuation in the electron density on scales comparable to the outer scale is ΔN_{e}, then the rms scattering angle due to these scales is given by

$$\theta_{\mathrm{scatt}}(r_{\mathrm{out}}) \sim r_{\mathrm{e}}\lambda^2\left(\frac{L}{r_{\mathrm{out}}}\right)^{1/2}\Delta N_{\mathrm{e}}, \qquad (4)$$

where L/r_{out} is the screen thickness expressed in units of r_{out}. For a Kolmogorov spectrum, the scattering angle increases with decreasing lengthscale as the inverse one-sixth power of the scale. Therefore the scattering angle reaches a maximum at the smallest scale present in the spectrum, namely the inner scale r_{in} (provided $r_{in} > r_{diff}$). Setting the maximum scattering angle to the observed angular sizes of Cyg X-3 at the two frequencies of our observations, and using $L/r_{out} \sim 10$, we find that

$$\Delta N_e \sim 10^2 \left(\frac{r_{in}}{10^5\ \mathrm{km}}\right)^{1/6} \mathrm{cm}^{-3}. \quad (5)$$

We expect that ΔN_e is of the same order as the mean electron density N_e in the scattering screen, and we therefore estimate that $N_e \lesssim 100$ electrons cm^{-3}, with a weak dependence on the inner scale. Assuming that the local magnetic field is in equipartition with the ionized material, we also estimate a field strength of

$$B \sim 10^{-4} \left(\frac{r_{in}}{10^5\ \mathrm{km}}\right)^{1/12} \left(\frac{T}{10^4\ \mathrm{K}}\right)^{1/2} \mathrm{G}, \quad (6)$$

where a temperature $T \sim 10^4$ K is appropriate if the scattering screen is part of an H II region in the Cygnus OB association. The lateral extent of the scattering screen has to be at least several outer scales in order to produce the full 408-MHz image (which covers many r_{out}). In fact, if we do not wish to say that the line of sight just happened to be perfectly aligned with a blob of enhanced scattering, we must assume that the scattering screen extends laterally over distances much greater than the size of the projected image. We thus deduce that the scattering screen must be essentially sheet-like in structure. We do not speculate here on the nature of this sheet of high electron density or on the source of its ionization.

It is worth noting that all of our results refer to the particular line of sight towards Cyg X-3 that is known to produce unusually large scattering. While it is reasonable to assume that these results, especially the small outer scale, would apply to other strongly scattered lines of sight, it is not clear that they are relevant for less extreme regions of the ISM. In particular, it is quite possible that the bulk of the ISM has a much larger outer scale, perhaps even as large as hundreds of parsecs (e.g. Armstrong, Cordes & Rickett 1981).

4 THE INNER SCALE OF TURBULENCE

An important lengthscale in any turbulent spectrum is the inner scale, the lengthscale at which the turbulent energy is dissipated and below which the spectrum cuts off. Coles et al. (1987) proposed that if the inner scale of interstellar turbulence is $\sim 10^5$ km, then some of the observations of scintillation of radio sources could be explained. Despite considerable observational effort (see Rickett 1990 for a review), there has been no direct and clear-cut determination of the inner scale from scattering data for any individual line of sight. However, a few studies have combined the results from many lines of sight to obtain an estimate of the inner scale. Rickett & Lyne (1990) explained the amplitude of 'refractive' scintillation in the Crab pulsar and other radio pulsars by means of an overall Kolmogorov spectrum of density fluctuations in the ISM with an inner scale $\sim 10^6$ km. Spangler & Gwinn (1990) combined interferometric data on a number of scatter-broadened sources to estimate an inner scale in the range 50–200 km, but Rickett (1990) warns that there are some systematic effects which could invalidate this result. Finally, Gupta, Rickett & Coles (1993) have obtained an estimate of $\sim 10^4$–10^6 km, using pulsar scintillation data at 74 MHz. Our high-quality data on Cyg X-3, combined with other recent observations, provide the best opportunity so far for constraining the inner scale for an individual line of sight. The analysis we present here is based on the theory developed by GN89 but, since their discussion is highly technical, we summarize the relevant parts of the theory before going on to discuss the Cyg X-3 data.

4.1 Summary of the theory

4.1.1 Scales and image regimes

For an interferometer whose phase centre is fixed at the true position of a point source, the mean visibility on baseline b, averaged over many independent realizations of the scattering screen, is given by (Rickett 1977, 1990; Tatarskii & Zavorotnyi 1980)

$$\langle V(b)\rangle = \exp\left[-\frac{1}{2} D_\phi(b)\right], \quad (7)$$

where $D_\phi(b)$ is the phase structure function, the mean square phase difference between two lines of sight separated by a distance b:

$$D_\phi(b) = \langle[\phi(r+b) - \phi(r)]^2\rangle_r. \quad (8)$$

The phase fluctuation $\phi(r)$ at transverse position r can be calculated as an integral of the electron density N_e over the line of sight:

$$\phi(r) = r_e \lambda \int_{z_{min}}^{z_{max}} N_e(r, z)\, \mathrm{d}z, \quad (9)$$

where $r_e = e^2/m_e c^2$ is the classical electron radius, λ is the wavelength of the radiation, z measures distance away from the observer, and the scattering screen extends from z_{min} to z_{max}. Fluctuations in $\phi(r)$ arise because of spatial variations in $N_e(r, z)$. In the case of Cyg X-3, we have argued that the scattering screen is very thin compared with the distance from the observer to the screen and the screen to the source. Therefore we assume a thin phase-changing scattering screen rather than an extended scattering medium (Romani et al. 1986). Moreover, since the distance to the source (~ 10 kpc) is much greater than the distance to the screen (~ 2 kpc), it is not necessary to include spherical effects (Rickett 1990).

Density fluctuations in the ISM are believed to occur over a wide range of scales, and it is usually assumed that they are caused by some kind of a turbulent cascade. It is therefore reasonable to think that the spectrum of fluctuations will take the form of a power law as a function of wave-vector (Lovelace 1970). The three-dimensional density fluctuation power spectrum can thus be modelled as

$$P_{3N}(\boldsymbol{q}) = C_N^2 |\boldsymbol{q}|^{-\beta}, \qquad q_{out} \lesssim |\boldsymbol{q}| \lesssim q_{in}, \quad (10)$$

where $q_{out} = 1/r_{out}$ and $q_{in} = 1/r_{in}$ are wave-vectors corresponding to the outer and inner scales, respectively, the largest and smallest scales present. The parameter C_N^2 describes the normalization of the spectrum .

Following GN89, we model the effects of the spectrum given in equation (10) by means of a structure function,

$$D_\phi(b) = C\lambda^2[(b^2 + r_{in}^2)^{\alpha/2} - r_{in}^\alpha], \qquad \alpha \equiv \beta - 2. \tag{11}$$

Note that in some of the literature the index that we have identified as β is referred to as α; the notation adopted here agrees with that used by Rickett (1990). The constant C measures the amplitude of the integrated density fluctuations, and we have explicitly included the λ-dependence according to equation (9).

In the theory of interstellar scattering and scintillation, a distinction is made between 'shallow' and 'steep' spectra (Blandford & Narayan 1985; Goodman & Narayan 1985; Narayan 1988; Rickett 1990); the former correspond to $\beta < 4$ and the latter to $\beta > 4$. The principal distinction is that for shallow spectra the angular scattering increases as the scale decreases (i.e. increasing q), while for steep spectra it is the largest scales that dominate. For shallow spectra, therefore, the angular size of the image is determined primarily by the scattering associated with the smallest relevant scales, either the inner scale r_{in} or the diffractive scale r_{diff} defined below. There are significant differences between the physics of wave propagation in the two cases and several clearly identified differences in their observational signatures. The weight of the evidence so far is that the ISM has a shallow spectrum of density fluctuations. In Section 4.2.3, we present yet another piece of evidence, based on our Cyg X-3 data, in support of this conclusion. However, several pulsars exhibit phenomena such as drifting bands and quasi-periodic structure in their dynamic spectra, which apparently require more power at long wavelengths than shallow spectra can provide (Hewish 1980; Roberts & Ables 1982; Hewish, Wolszczan & Graham 1985). These observations suggest a steep spectrum, in conflict with the bulk of the evidence.

One of the goals of radio observations of interstellar scattering is to determine the value of the exponent β. Although the observations clearly indicate values smaller than 4, a precise determination of this exponent has not yet been possible. In general, the data suggest a value somewhere in the range ~3.5–3.8 (e.g. Gwinn, Moran & Reid 1988a; Gwinn et al. 1988b,c; Spangler & Cordes 1988; Mutel & Lestrade 1990). From our Cyg X-3 data we find a limit $\beta < 3.81$ (Section 4.2.3) which is consistent with these results. Given this situation, it is the usual practice to assume that the spectrum corresponds to that predicted for Kolmogorov turbulence, as originally proposed by Lee & Jokipii (1976) and Armstrong et al. (1981). This gives $\beta = 11/3$, $\alpha = 5/3$, and we assume these values in most of the following discussion.

The particular functional form in equation (11) is not rigorously equivalent to equation (10), but it represents a convenient way of introducing the qualitative features of a cut-off at small scales. Note that we have not explicitly introduced an outer scale into equation (11), because for the Kolmogorov spectrum, which is a shallow spectrum, the scattering is dominated by density fluctuations on small lengthscales. Therefore, for all of the discussion in this section, the precise value of the outer scale is irrelevant, and equation (11) effectively assumes that $r_{out} \to \infty$.

The *diffractive scale* r_{diff} is a measure of the transverse coherence scale of the radiation field at the observer and determines the angular size θ of the scatter-broadened image. It is convenient to define r_{diff} by the condition

$$D_\phi(r_{diff}) = 1. \tag{12}$$

r_{diff} is thus the baseline on which the visibility drops to a value of $1/\sqrt{e}$ (see equation 7). If we assume a Gaussian image profile, then we have $D_\phi(b) = b^2/r_{diff}^2$. Substituting this in equation (7), it is easily shown that the FWHM of the image is related to r_{diff} by

$$\theta_{FWHM} = 7.73 \times 10^4 \frac{\lambda}{r_{diff}} \text{ arcsec.} \tag{13}$$

A second important scale is the *Fresnel scale*,

$$r_F = \sqrt{\lambda D/2\pi}. \tag{14}$$

Combining r_{diff} and r_F, we can then define a third scale, the *refractive scale*,

$$r_{ref} = r_F^2/r_{diff} \sim D\theta, \tag{15}$$

which is the linear size of the scattered image as projected on the scattering screen at distance D. If the relative motion between the Earth-source line and the scattering material is v, then we may define analogous time-scales,

$$t_{diff} = r_{diff}/v, \qquad t_{ref} = r_{ref}/v. \tag{16}$$

These describe the characteristic time-scales of diffractive and refractive scintillation. We may also define a diffractive bandwidth $\Delta\nu_{diff}$ and a critical source size θ_{diff} by

$$\Delta\nu_{diff} = cr_{diff}^2/\lambda^2 D, \tag{17}$$

$$\theta_{diff} = r_{diff}/D. \tag{18}$$

$\Delta\nu_{diff}$ is the bandwidth over which diffractive scintillation is coherent, and θ_{diff} is the source angular size above which diffractive scintillation is quenched.

Narayan & Goodman (1989) showed that, in strong scattering (i.e. $r_{diff} \ll r_F$) which is relevant for the ISM at centimetric and longer wavelengths, imaging can be classified into three regimes: (i) the Snapshot Image regime; (ii) the Average Image regime and (iii) the Ensemble-Average Image regime. Which of these regimes is relevant depends on the integration time and bandwidth of the observations, and the intrinsic angular size of the source. Let the observations be made with a bandwidth $\Delta\nu$ and integration time t_{int}, and let the intrinsic, unscattered, angular size of the source be θ_s. GN89 showed that the observations will correspond to the Snapshot Image regime if all three of the following conditions are simultaneously met, namely

$$t_{int} < t_{diff}, \qquad \Delta\nu < \Delta\nu_{diff}, \qquad \theta_s < \theta_{diff}. \tag{19}$$

The Average Image regime is when one or more of the conditions in equations (19) is violated, but all three of the following are satisfied, viz.

$$t_{int} < t_{ref}, \qquad \Delta\nu < \nu = c/\lambda, \qquad \theta_s < \lambda/b_{max}, \tag{20}$$

where b_{max} is the longest baseline used in the observations. Finally, the Ensemble Average image regime is when one or more of the conditions in equations (20) is violated. Taking the distance to the scattering screen to be $D = 2$ kpc, we have for our Cyg X-3 observations the following lengthscales,

$$\begin{aligned} &408\ \text{MHz:}\ r_{diff} = 2.0\times10^{1}\ \text{km}, \quad r_F = 2.7\times10^{6}\ \text{km}, \\ &\qquad r_{ref} = 3.6\times10^{11}\ \text{km}, \\ &1692\ \text{MHz:}\ r_{diff} = 9.1\times10^{1}\ \text{km}, \quad r_F = 1.3\times10^{6}\ \text{km}, \\ &\qquad r_{ref} = 1.9\times10^{10}\ \text{km}. \end{aligned} \tag{21}$$

Writing $v = 30 v_{30}$ km s^{-1}, the relevant time-scales are

$$\begin{aligned} &408\ \text{MHz:}\ t_{diff} = 0.7 v_{30}^{-1}\ \text{s}, \quad t_{ref} = 300 v_{30}^{-1}\ \text{yr}, \\ &1692\ \text{MHz:}\ t_{diff} = 3 v_{30}^{-1}\ \text{s}, \quad t_{ref} = 20 v_{30}^{-1}\ \text{yr}. \end{aligned} \tag{22}$$

Similarly, the critical bandwidth and source sizes are

$$\begin{aligned} &408\ \text{MHz:}\ \Delta\nu_{diff} = 0.0036\ \text{Hz}, \quad \theta_{diff} = 6.5\times10^{-8}\ \text{mas}, \\ &\qquad \lambda/b_{max} = 1.1\ \text{arcsec}, \\ &1692\ \text{MHz:}\ \Delta\nu_{diff} = 1.3\ \text{Hz}, \quad \theta_{diff} = 2.9\times10^{-7}\ \text{mas}, \\ &\qquad \lambda/b_{max} = 0.16\ \text{arcsec}. \end{aligned} \tag{23}$$

For the observations on Cyg X-3, there are two time-scales that we can consider, namely the coherent integration time for each measured visibility t_{coh}, and the total duration of the observations t_{tot}. The relevant bandwidth $\Delta\nu_{obs}$ is that used to make the observations, while the source size may be estimated by taking an expansion velocity of $\sim$ 10 mas d^{-1} and multiplying it by the number of days since the start of the outburst. We thus have

$$\begin{aligned} &408\ \text{MHz:}\ t_{coh} = 320\ \text{s}, \quad t_{tot} = 17\ \text{h}, \\ &\qquad \Delta\nu = 5\ \text{MHz}, \quad \theta_s \sim 50\ \text{mas}, \\ &1692\ \text{MHz:}\ t_{coh} = 600\ \text{s}, \quad t_{tot} = 25\ \text{h}, \\ &\qquad \Delta\nu = 10\ \text{MHz}, \quad \theta_s \sim 20\ \text{mas}. \end{aligned} \tag{24}$$

Comparing the numbers in equations (24) with those in equations (22) and (23), we see that all of the inequalities in (19) are violated, while all the inequalities in (20) are satisfied. We thus conclude that our observations of Cyg X-3 correspond to the Average Image regime.

4.1.2 *The wavelength dependence of scatter-broadening*

The structure function in equation (11) has two different asymptotic behaviours, depending on whether $b \gg r_{in}$ or $b \ll r_{in}$:

$$\begin{aligned} &D_\phi(b) \rightarrow C\lambda^2 b^\alpha = C\lambda^2 b^{5/3}, \quad b \gg r_{in}, \\ &D_\phi(b) \rightarrow (\alpha/2)\, C\lambda^2 r_{in}^{-1/3} b^2 = (5/6)\, C\lambda^2 r_{in}^{-1/3} b^2, \quad b \ll r_{in}, \end{aligned} \tag{25}$$

where the second relation in each equation is obtained by assuming a Kolmogorov spectrum ($\beta = 11/3$, $\alpha = 5/3$). Therefore, when we solve equation (12), we obtain two different asymptotic dependences of r_{diff} on λ, depending on the relative magnitudes of r_{diff} and r_{in}, namely

$$\begin{aligned} &r_{diff} \propto \lambda^{-2/\alpha} = \lambda^{-6/5}, \quad r_{in} \ll r_{diff}, \\ &r_{diff} \propto \lambda^{-1}, \quad r_{in} \gg r_{diff}. \end{aligned} \tag{26}$$

Thus, substituting in equation (13), we see that

$$\begin{aligned} &\theta_{FWHM} \propto \lambda^{\beta/\alpha} = \lambda^{11/5}, \quad r_{in} \ll r_{diff}, \\ &\theta_{FWHM} \propto \lambda^2, \quad r_{in} \gg r_{diff}. \end{aligned} \tag{27}$$

There is, of course, a smooth transition from one scaling to the other when $r_{in} \sim r_{diff}$. Equations (27) suggest that, by measuring the variation of θ_{FWHM} versus λ for a scattered source, it may be possible to estimate r_{in}, or at least to set a limit on it. We attempt to do this, using data on Cyg X-3, in Section 4.2.

4.1.3 *The visibility as a function of baseline* $\lesssim r_{diff}$

Another method to estimate r_{in} is based on the form of $\langle V(b)\rangle$ given in equation (7) and the fact that the structure function has the two different asymptotic behaviours given in equations (25). Thus, if the visibilities are found to vary as $\exp[-(b/r_{diff})^\alpha]$, with $\alpha < 2$, we may deduce that r_{in} is smaller than the baselines being considered. The particular value of α obtained from the fit would be a measurement of the index of the turbulence spectrum. Alternatively, if $V(b) \propto \exp[-(b/r_{diff})^2]$, then $r_{in} \gg b$. Finally, if r_{in} is comparable to the baselines being considered, then there will be a smooth transition between the two scalings. This means that a careful measurement of the shape of $V(b)$, particularly on baselines $b \sim r_{diff}$, can provide information on r_{in}.

Gwinn et al. (1988a,c), Spangler & Cordes (1988), Moran et al. (1990), Mutel & Lestrade (1990) and Lo et al. (1993) have effectively determined the exponent of b/r_{diff}, using a variety of different fitting methods to their visibility data. One simple way to analyse the visibility is to plot $\log\{-\ln[V(b)]\}$ against $\log(b)$ and to fit a straight line to the data. If $b \ll r_{in}$, then the slope will be 2.0 (corresponding to a pure Gaussian scattering disc), while if $b \gg r_{in}$, then the slope will be 1.67 in the case of a Kolmogorov spectrum, or some other value less than 2 for a more general shallow spectrum. Any particular set of interferometer observations will not span a large enough range of b to detect the changing slope, even if the baselines are comparable to r_{in}. Hence, to use this method to constrain r_{in}, one will need to combine the results from different observations of an individual source. We discuss the analysis of $V(b)$ at 408 MHz and at 1692 MHz for Cyg X-3 in Section 4.2.2.

4.1.4 *Fluctuations in the visibility on baselines* $\gg r_{diff}$

A final method to estimate r_{in} is based on the behaviour of the visibilities for baselines $b \gg r_{diff}$. For such baselines the expectation value $\langle V(b)\rangle$ of the complex visibility averaged over many realizations of the scattering screen is exponentially small, as shown by equation (7). However, GN89 showed that in the Average Image regime there are random fluctuations, superimposed on the mean visibilities, which vary from one independent realization of the scattering material to the next. This fluctuating power corresponds to low-level granulation of the scattered image on angular scales smaller than θ_{FWHM}.

Following GN89, let us define the following rms fluctuation in the visibility on a baseline b:

$$\delta V_a(b) = [\langle |V(b) - \langle V(b)\rangle|^2\rangle_a]^{1/2} = [\langle |V_a(b)|^2\rangle - \langle V(b)\rangle^2]^{1/2}, \tag{28}$$

where the subscript a is to remind us that the fluctuations correspond to the Average Image. GN89 wrote down a general result for $|V_a(b)|^2$, expressed as an integral of a function of $D_\phi(b)$ (their equations 2.5.12 and 2.5.13). They also derived asymptotic expressions for $\delta V_a(b)$ for $b \gg r_{diff}$ (their equations 5.1.2 and 5.1.4). More recently, Goodman (1993, unpublished) has numerically evaluated $\delta V_a(b)$ for a number of power spectra relevant to the ISM, and has supplied his results in the form of numerical tables. We have used the tabulated values in our calculations.

For a structure function of the form assumed in equation (11), the form of $\delta V_a(b)$ depends on the value of α and the two dimensionless ratios, r_F/r_{diff} and r_{in}/r_{diff}. Fig. 7 shows a typical set of results for the case when $\log(r_F/r_{diff}) = 5$, which corresponds very nearly to the 408-MHz observations (see equations 21). In Fig. 7(a), we assume that the inner scale is much smaller than the diffractive scale, and show how the average image fluctuations $\delta V_a(b)$ vary as a function of α. We see that the power due to image granulation increases rapidly with increasing α. In Fig. 7(b), we take a specific value for α, namely the Kolmogorov value of 5/3, and show how $\delta V_a(b)$ varies as a function of the inner scale. We see that the amplitude of the visibility fluctuations increases monotonically with increasing r_{in}.

These results show that by measuring the excess power in the visibilities predicted by GN89 it is possible to obtain useful information on the spectrum of interstellar turbulence, although the dependence of $\delta V_a(b)$ on α is qualitatively similar to that on r_{in} and so it is not possible to obtain both simultaneously. If we assume a value of r_{in}, we can obtain an estimate of α, and vice versa. We use both approaches in Section 4.2.3, when we analyse the MERLIN data on Cyg X-3. First, we assume r_{in} to be arbitrarily small and thereby obtain an upper limit on α. We then set α equal to

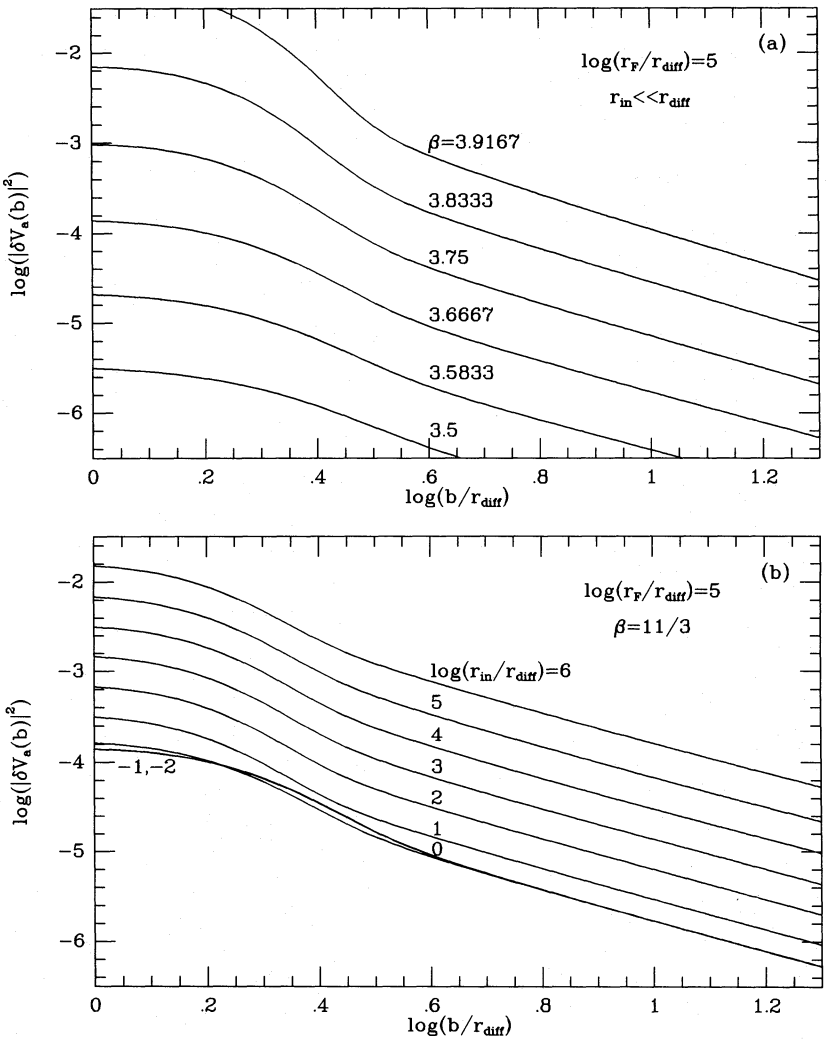

Figure 7. Theoretical estimates of the mean square fluctuation in the visibility, $|\delta V_a(b)|^2$, as a function of b/r_{diff} for a scatter-broadened source in the Average Image regime. (a) shows the effect of varying the spectral exponent β for a case when $\log(r_F/r_{diff}) = 5$ and $r_{in} \ll r_{diff}$; the cases shown correspond to $\beta = 3.5$, 3.5833, 3.6667, 3.75, 3.8333 and 3.9167. (b) shows the effect of varying the inner scale r_{in} for a case when $\beta = 11/3$ and $\log(r_F/r_{diff}) = 5$. The cases shown correspond to $\log(r_{in}/r_F) = -2, -1, 0, 1, 2, 3, 4, 5$ and 6 (curves derived from tables provided by J. Goodman, private communication).

the Kolmogorov value and thus obtain an estimate of the inner scale. Mutel & Lestrade (1990) were the first to measure $\delta V_a(b)$ for any source. While they could conclude that their 0.16-m VLBI observations of the radio source 2005+403 were consistent with a Kolmogorov spectrum, their data were not of sufficient quality to enable them to constrain r_{in}.

Before closing this section we draw attention to some complications in applying the image granulation analysis to actual data. The numerical estimates of $\delta V_a(b)$ computed by Goodman and shown in Fig. 7 include fluctuations in $V(b)$ from all causes. In particular, they include contributions from such 'refractive effects' as refractive scintillation, wander of the centroid of the image, and fluctuations in the mean scattering size (Romani et al. 1986). In fact, the refractive effects are filtered out of our data, since the zero-baseline flux density, the position of the image centroid, and the mean size of the scatter-broadened image are all fitted when computing the mean visibility. This means that the visibility fluctuation power in the data will be less than that predicted by the theory, especially at small baselines $b \sim r_{diff}$. We have therefore restricted our analysis to baselines $b \gtrsim 3r_{diff}$, where the effect of the image fitting is expected to be negligible.

The other complication is that the GN89 theory of image granularity was developed on the basis of a homogeneous isotropic scattering screen, whereas we now know that the scattering can be significantly anisotropic. We explicitly allow for this anisotropy by making r_{diff} and the ratio r_{in}/r_{diff} functions of position angle in the sky (see Section 4.2.3), which should help to model some of the effect. Unfortunately, the anisotropy is not even homogeneous, since in our model we think that the 408-MHz image extends over several independent patches of magnetic field with different orientations of the anisotropy. We expect that this will introduce some additional fluctuation power in the visibilities at long baselines. Another potential complication is that the normalization constants C_N^2 and C in equations (10) and (11) may not be spatially constant, but may vary across the image, especially on scales larger than r_{out}. This will cause additional structure in the image (e.g. Hewish 1992) and produce excess power in the visibilities. We have not attempted to estimate the magnitude of these effects and therefore, in Section 4.2.3, we obtain an upper bound on r_{in} rather than a precise determination of its value.

A third potential complication is, in fact, not an issue for our particular data set. GN89 showed that, in addition to the low-level modulation in the Average Image regime which is caused by refractive effects, there is also order-unity modulation in the Snapshot Image regime due to diffractive speckles. Even when one is in the Average Image regime, it is possible to have some residual power due to the diffractive speckles which may interfere with the measurement of the refractive power. In our case, this is not a problem, because the diffractive speckles are averaged to an extremely large degree. By comparing equations (24) and (23) we see that the observing bandwidth is much larger than the critical bandwidth $\Delta\nu_{diff}$, and that the source size is very much larger than the critical size θ_{diff}. Both of these effects will smooth the snapshot speckles by a very large factor. We therefore do not believe that there can be any measurable effects in our data due to diffractive speckles.

4.2 Application of the theory to Cyg X-3

4.2.1 *The wavelength dependence of scatter-broadening*

There have been several measurements of the size of the scatter-broadened image of Cyg X-3 in addition to those presented in this paper. The most useful measurements are summarized in Table 2. The interpretation of the angular broadening data is, however, complicated by the fact that the scattering is now known to be anisotropic. The $\lambda = 0.06$-m (5-GHz) results of Schalinski et al. (1994) are consistent with the same ellipticity as seen in the 1692-MHz image and in the same p.a., whereas at $\lambda = 0.207$ m (1452 MHz) and $\lambda = 0.0135$ m (22.2 GHz) Molnar et al. (1988) only determined single equivalent Gaussian diameters. Where the image is known to be elliptical we use the mean FWHM, $\theta_{mean} = (\theta_{max}\theta_{min})^{1/2}$. It is reasonable to assume that the ellipticity of the image at 1452 MHz is similar to that at 1692 MHz, and that Molnar et al.'s fitted diameter corresponds to θ_{mean}. For lack of other evidence, we also assume that the diameter at 22.2 GHz corresponds to θ_{mean}.

The fractional uncertainties on the three longest wavelength measurements of θ_{mean} are typically a few per cent, whereas those on the shortest two wavelengths – where it is harder to disentangle the effects of intrinsic source structure – are an order of magnitude higher. Clearly, it would be very helpful to obtain better scattering data at frequencies above 1.69 GHz.

We have attempted to use the data in Table 2 to determine r_{in} for the scattering medium in the direction towards Cyg X-3. Following equations (27), we made a least squares fit of the θ_{mean} data to the two asymptotic relations $\theta_{mean} \propto \lambda^{11/5}$ and $\theta_{mean} \propto \lambda^2$ appropriate for a Kolmogorov spectrum. Neither gives a good fit; $\chi^2 = 69.6$ for the $\lambda^{11/5}$ fit and 18.7 for the λ^2 fit. These are to be compared to the expected $\chi^2 = 4$ for the number of degrees of freedom. The two fits are shown in Fig. 8. We then tried a fit of the form λ^γ, allowing γ to be a free parameter. The best fit was obtained for $\gamma = 2.055$, consistent with the two-wavelength fits of Wilkinson et al. (1988) and Schalinski et al. (1993). $\gamma = 2.055$ gave $\chi^2 = 10.2$, but even this fit is not acceptable for three degrees of freedom. The optimum γ can be interpreted in two ways. We could assume that $r_{in} \ll r_{diff}$ and use the first of equations (27) to deduce that $\beta = 3.9$; although, as we mentioned earlier, there are several independent indications that $\beta < 3.8$ (see also Section 4.2.3). We therefore prefer the second alternative, namely that $\alpha = 5/3$, and that the small deviation of γ from the value 2 may be an indication that the inner scale lies within the range of the baselines used to measure the data. To investigate this option we carried out a more detailed analysis.

The structure function we have assumed has the form given in equation (11), with α assumed to be equal to 5/3 and two additional parameters, namely C and r_{in}. For any choice of C and r_{in}, we can solve equation (12) to obtain r_{diff} as a function of λ. Substituting this in equation (13), we may then calculate the FWHM of the scatter-broadened image as a function of λ. By comparing the calculated values with the observed θ_{mean} values listed in Table 2, we can optimize C and r_{in}. We carried out these calculations as follows. For each value of r_{in}, we adjusted C until the calculated values of θ_{FWHM} at the observed wavelengths gave the best fit to the data. At this value of C, we calculated the χ^2 corresponding

to the deviations between the model and the data. Fig. 9 shows the resulting χ^2 as a function of r_{in}. The shape of this curve is consistent with the results described in the previous paragraph. For $r_{in} \ll b_{min} \sim 10^1$ km, the model behaves exactly as the $\theta \propto \lambda^{11/5}$ asymptotic model, and so the χ^2 has a value of 69.6. Similarly, for $r_{in} \gg b_{max} \sim 10^3$ km, the behaviour is like the other asymptotic model, $\theta \propto \lambda^2$, and so we get a χ^2 of 18.7. Between these two limits, χ^2 dips to a minimum value of 7.4 at $r_{in} \sim 6 \times 10^1$ km. This value of χ^2 is to be compared with the expected value of 3 (five data values minus two parameters). Thus, although the model with $r_{in} = 6 \times 10^1$ km is superior to all other models we have tried, its χ^2 is still unacceptably large.

Table 2. Mean Gaussian diameters (FWHM) of Cyg X-3 at different wavelengths. The references are 1: this paper; 2: Molnar, Reid & Grindlay (1988); 3: Schalinski et al. (1994).

Wavelength (m)	θ_{mean} (arcsec)	r_{diff} (km)	Ref.
0.735	2.91 ± 0.07	20 ± 0.5	1
0.207	0.229 ± 0.005	70 ± 2	2
0.177	0.150 ± 0.005	91 ± 3	1
0.060	0.018 ± 0.006	258 ± 86	3
0.0135	0.00068 ± 0.00008	1535 ± 254	2

Before interpreting the results, we need to ask why we have been unable to find any model with a χ^2 value within the normally acceptable range. The simplest explanation is, of course, that our estimates of the uncertainties in the θ_{mean} values are too optimistic. While this may be true for some of the other data in Table 2, we have been rather conservative in the error estimates we quote at 0.735 and 0.117 m. The other possibility is that there are systematic errors due to the image anisotropy. Only the 0.735- and 0.177-m data described in this paper have been properly analysed, including the effects of anisotropy. In the case of the other three values in Table 2, it is no more than an educated guess that the quoted θ values refer to the geometric mean θ_{mean}. Furthermore, even if the data do refer to the true θ_{mean}, there is no guarantee that θ_{mean} will follow the asymptotic scalings in equations (27), since the scalings have been derived for an isotropic scattering model. This is particularly an issue at the longer wavelengths, where the anisotropy varies as a function of λ.

Despite the uncertainties discussed above, we feel that we can certainly reject any value of $r_{in} \lesssim 10^1$ km, since in this case χ^2 is much too large. However, we are not inclined to reject values of r_{in} at the upper end of the range shown in Fig. 9, since χ^2 is only a little larger than the minimum value we obtained. Therefore the only conclusion we can draw from this analysis of current data is that $r_{in} > 10$ km.

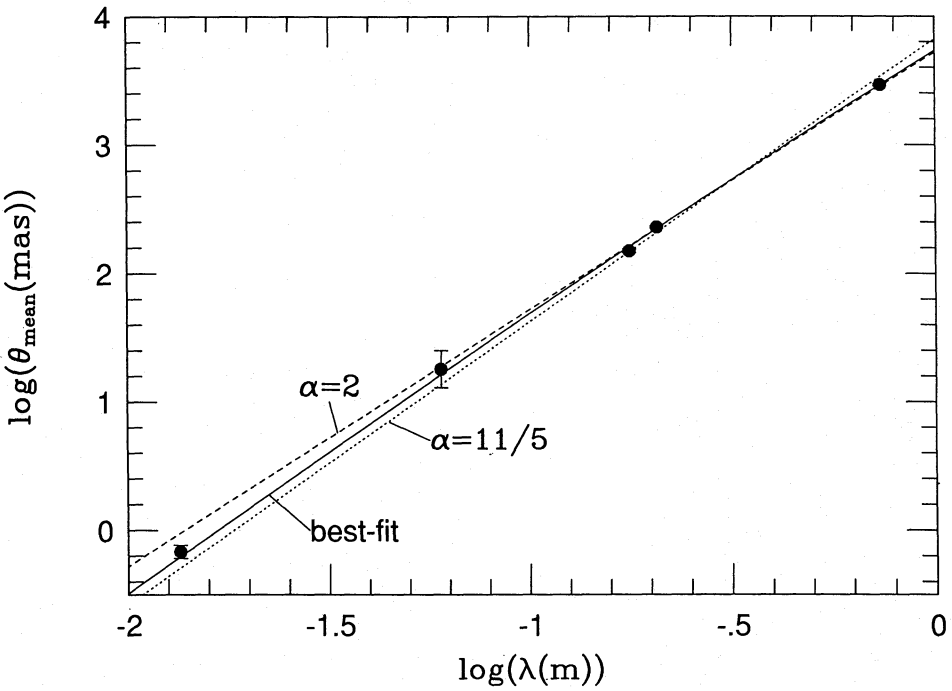

Figure 8. Three models for the variation of θ_{mean} with λ, compared with the observations. The dashed and dotted lines represent models of the form $\theta_{mean} \propto \lambda^2$ and $\theta_{mean} \propto \lambda^{11/5}$, respectively. The solid line is our best model and corresponds to the χ^2 minimum in Fig. 9.

4.2.2 *The visibility as a function of baseline* $\lesssim r_{\rm diff}$

The fact that the data at both 408 and 1692 MHz are fitted reasonably well by simple elliptical Gaussian models immediately suggested that $\alpha \approx 2$. However, in order to be more quantitative, we follow the analysis method described in Section 4.1.3. In Fig. 10, we show the plot of $\log\{-\ln[V(b)]\}$ against $\log(b)$ for the 408-MHz data; in making this plot we have averaged the visibility data over all position angles. As we discussed in Section 2.1, the source is 99 per cent resolved on baselines $b > 60$ km; at these long baselines the points deviate markedly from a straight line, corresponding to an excess of power compared with an exponential decay of $V(b)$. This excess is due to a combination of the higher order scattering effects described in Section 4.1.4 and Ricean noise bias on the visibility amplitudes. We therefore exclude these long-baseline data from this part of the analysis. (We discuss a high-SNR subset of the long baselines in detail in the next section.)

Since our analysis is in terms of the normalized visibility $V(b)$, we needed to adopt a value for the zero-baseline flux density (S_0) with which to divide the run of correlated flux density shown in Fig. 1. Incorrect values of S_0 produce curvature in the $\log\{-\ln[V(b)]\}$ against $\log(b)$ plot, and we therefore produced a series of such plots for different values of S_0 (varying by only a few per cent from our by-eye estimate from Fig. 1) and used the χ^2 statistic to determine which of them produced the best straight line. The slope of the best-fitting straight line is sensitive to removal of curvature from the plot, and hence some care was taken over this part of the procedure.

Given the subtlety of the behaviour we are investigating, we tested the software with simulated MERLIN data. We started by assuming a circular Gaussian source and added pure Gaussian noise to the visibilities of a magnitude similar to that in the actual data. In the $\log\{-\ln[V(b)]\}$ against $\log(b)$ plot we again deleted the longer baseline data. The value of χ^2 corresponding to the best-fitting straight line was comparable with the number of degrees of freedom (the number of points on the plot minus one); this fact, coupled with an examination of the post-fit residuals, confirmed that the simulated data were well represented by a straight line, and that the known scatter on $V(b)$ was being properly represented in the plot. From the residuals and the variation in χ^2 as we varied S_0, we confirmed that the correct value of S_0 could be recovered with an accuracy significantly better than 1 per cent. The best-fitting straight line slope had the expected value of 2.00 with an uncertainty of about 1 per cent, mostly determined by the range of acceptable S_0.

We then ran a series of simulations for Gaussian sources of different ellipticities and different u, v coverages - large

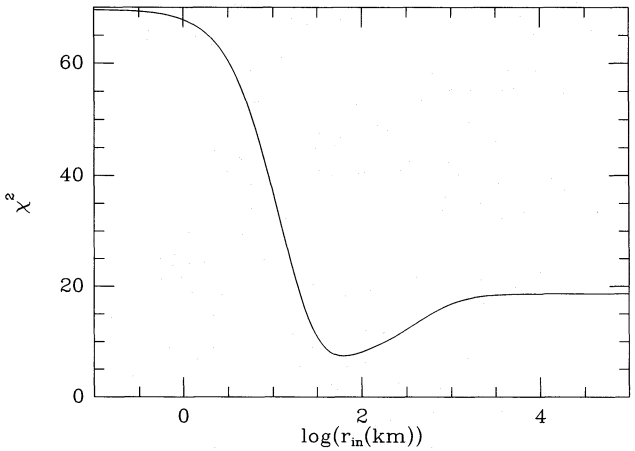

Figure 9. Results of fitting the observed $\theta_{\rm mean}$ versus λ. The figure shows the variation of the χ^2 of the fit as a function of the assumed inner scale $r_{\rm in}$. The best fit is obtained for $\log r_{\rm in} = 1.8$, but all values of $\log r_{\rm in} > 1$ are acceptable.

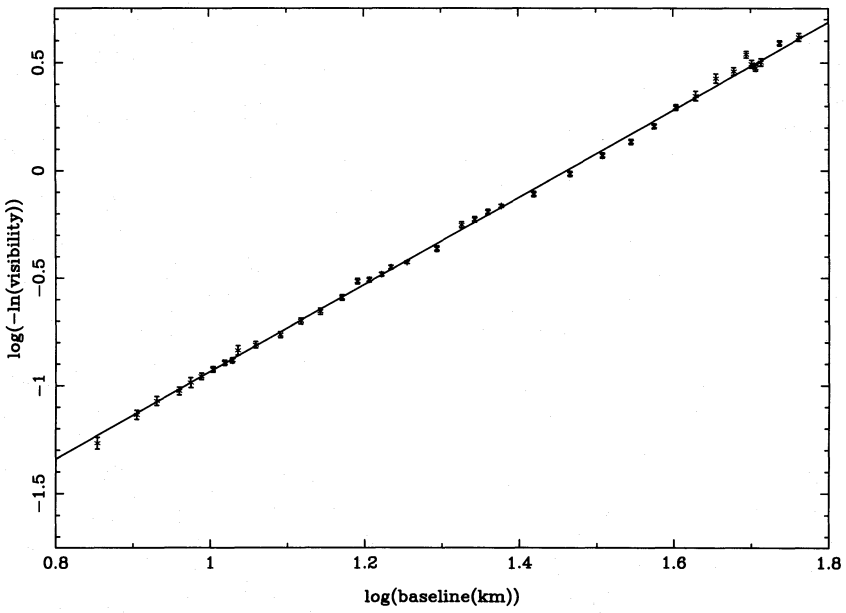

Figure 10. A plot of $\log\{-\ln[V(b)]\}$ against $\log(b)$ for the 408-MHz data averaged over all position angles. The best-fitting line has a slope of 2.03 ± 0.05.

sectors can be missing from MERLIN data for sources at low declinations or for high-declination sources if the hour angle coverage is limited. We suspected that the specific form of the u, v coverage might affect the results on elliptical sources, depending on the orientation of the ellipse with respect to the missing sector.

The action of averaging the data for an elliptical source over all position angles produces an increased scatter in the $\log\{-\ln[V(b)]\}$ against $\log(b)$ plot, and hence χ^2 is very much larger than the number of degrees of freedom. While the post-fit residuals are scattered on either side of zero, the simulated data have become statistically inconsistent with a straight line. Nevertheless, the correct S_0 could always be recovered as above. Most importantly, we found that the slope of the best-fitting line can be slightly, but significantly, biased below 2.0 with the effect increasing with ellipticity. For the mild ellipticities (0.88–0.76) found in the actual Cyg X-3 data, the slopes fell in the range 1.91–2.00. One obvious way around this problem is to average up $V(b)$ only in narrow sectors of the u–v plane, if possible aligned with the major and minor axes of the ellipse. This produces statistically better straight lines, but there remains a slight bias to lower values. From these simulations we concluded that a realistic uncertainty on the slope of the best-fitting line for our 408- and 1692-MHz data is ± 0.05. Slopes in the range 1.9–2.1 are therefore not significantly different from the pure Guassian value of 2.00.

We then returned to the actual data. Guided by the post-fit residuals, we found it necessary to delete one or two of the shortest baseline points before determining the best values of S_0 and the best-fitting lines. The slope of the best-fitting line for the data in Fig. 10 is 2.03 ($\chi^2 = 85$ for 39 degrees of freedom). Averaging of the data in the narrow u, v sector $90° \pm 20°$ (almost parallel to the minor axis of the scattered image) produced a slope of 2.10 ($\chi^2 = 26$ for 18 degrees of freedom). There were too few data to repeat the analysis along p.a. 0°. A previous analysis (Wilkinson et al. 1988) of these 408-MHz data (averaged over all angles) gave a slope of 1.88 ± 0.05, but we now believe that the slope cannot be reliably distinguished from 2.0.

The 1692-MHz data had better u, v coverage than the 408-MHz data. The slope of the best-fitting line for data averaged over all angles (shown in Fig. 11) was 1.93 ($\chi^2 = 464$ for 46 degrees of freedom); the slopes for data in the sectors $62° \pm 10°$ and $152° \pm 10°$ were 1.91 ($\chi^2 = 22$ for 10 degrees of freedom) and 1.97 ($\chi^2 = 1.2$ for six degrees of freedom), respectively.

In addition to the above analyses, we tried a different calculation where we allowed explicitly for the anisotropy of the image by renormalizing the baselines according to the best elliptical model fit, using the procedure described by Spangler & Cordes (1988). This allowed us to remove the effect of the anisotropy and to 'circularize' the image, so that we could analyse the whole data set for a single slope. We found a best-fitting slope of 1.96 for the 408-MHz data and 1.95 for the 1692-MHz data, which are not significantly different from the other results described above.

On the basis of all these analyses, we conclude that both the 408-MHz data and the 1692-MHz data are consistent with a slope of 2.00, i.e. that the profile of the scattering disc is Gaussian. This implies that $r_{\rm in} \gg r_{\rm diff}(1692\ {\rm MHz}) = 91$ km. However, since some of our calculated slopes are slightly below 2, and since we cannot rule out a slope as small as 1.9, we take a cautious view and weaken the constraint to $r_{\rm in} > 100$ km.

4.2.3 *Fluctuations in the visibility on baselines* $\gg r_{\rm diff}$

In this final method, we obtain a constraint on β and an estimate of $r_{\rm in}$ using the fluctuations in the visibilities on longer baselines. As discussed in Section 4.1.4, the most useful data for this purpose are those on baselines $b \gtrsim 3r_{\rm diff}$. Since the 1692-MHz data do not extend beyond $2.4r_{\rm diff}$, we had to ignore this data set. This is unfortunate, since the 1692-MHz data were of the highest quality. The 408-MHz data, on the other hand, extend out to $\sim 7r_{\rm diff}$ and are suitable for our analysis. In order to maximize the SNR, we retained only those visibilities which were measured on baselines involving the Lovell telescope. We thus have a total of 552 independent visibilities, of which 105 visibilities correspond to $b \gtrsim 3r_{\rm diff}$.

Our calculations proceed in two stages. For each assumed value of α and $r_{\rm in}$, we first use the low-b points, $b \lesssim 3r_{\rm diff}$, to fit $r_{\rm diff}$ and the other parameters of the mean image. Because of image anisotropy, $r_{\rm diff}$ is a function of position angle in the sky. To model this, we assume that $r_{\rm diff}$ varies as (see Narayan & Hubbard 1988 and appendix B of GN89)

$$r_{\rm diff}^2(\theta) = \frac{1}{2}(r_{\rm diff\,1}^2 + r_{\rm diff\,2}^2) + \frac{1}{2}(r_{\rm diff\,1}^2 - r_{\rm diff\,2}^2)\cos[2(\theta - \theta_0)], \tag{29}$$

which involves three parameters: $r_{\rm diff\,1}$, the diffractive scale corresponding to the major axis of the image, $r_{\rm diff\,2}$, the minor axis diffractive scale, and θ_0, the position angle of the major axis. Here θ is the position angle of the u, v point under consideration:

$$\theta = \tan^{-1}(v/u). \tag{30}$$

In this model, the locus of $r_{\rm diff}$ takes the form of an ellipse in a polar diagram in the u–v plane.

Using the low-b data, for each assumed value of $r_{\rm in}$ we fit four parameters, namely $r_{\rm diff\,1}$, $r_{\rm diff\,2}$, θ_0, and the zero-baseline flux density S_0. For each u, v point, we calculate $r_{\rm diff}$ through equation (29) and substitute this in equations (11) and (12) to obtain the structure function $D_\phi(b)$. We then calculate the correlated flux density predicted by the model for this baseline through equation (7), i.e.

$$S_{\rm calc}(u, v) = S_0 \exp\left[-\frac{1}{2}D_\phi(b)\right]. \tag{31}$$

By fitting the calculated values of $S_{\rm calc}(u, v)$ to the measured data on the short baselines, we determine the optimum set of parameters $r_{\rm diff\,1}$, $r_{\rm diff\,2}$, θ_0 and S_0 for the particular assumed value of $r_{\rm in}$. One complication is that the 'low-b' data on which this fit is done are defined such that $b \lesssim 3r_{\rm diff}$, but $r_{\rm diff}$ itself is known only after the parameters in equation (29) have been determined. We therefore have to iterate for self-consistency.

Having fitted the image shape using the low-b points, we then look at the fluctuating power on the high-b points. We normalize the absolute square of the fluctuation in the

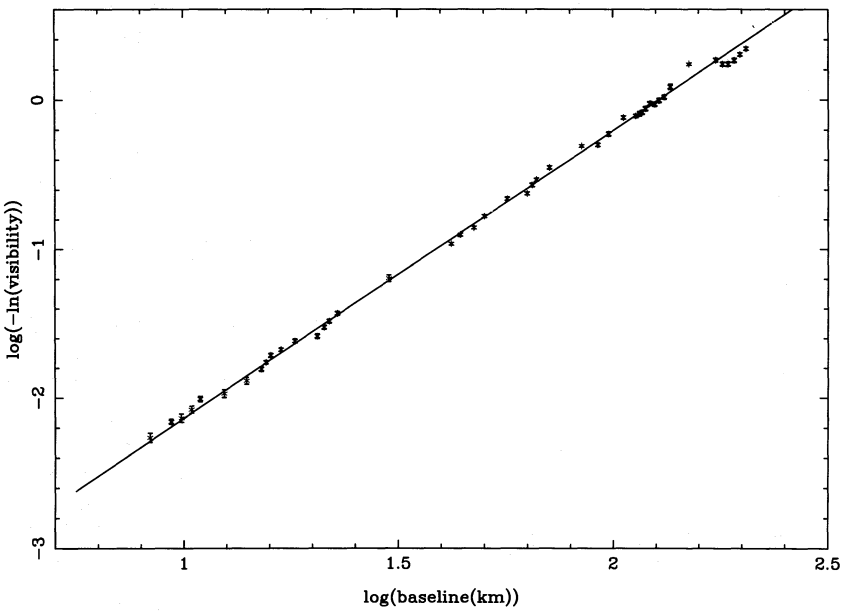

Figure 11. A plot of $\log\{-\ln[V(b)]\}$ against $\log(b)$ for the 1692-MHz data averaged over all position angles. The best-fitting line has a slope of 1.93 ± 0.05.

complex visibility by the expected variance according to the model and obtain a reduced χ^2 as follows:

$$\chi^2_{\rm red}(\beta, r_{\rm in}) = \frac{1}{2n_{>3}} \sum_{b>3r_{\rm diff}} \frac{|{\rm Re}[S_{\rm obs}(u,v)] - S_{\rm calc}(u,v)|^2 + |{\rm Im}[S_{\rm obs}(u,v)]|^2}{\sigma^2_{\rm m}(u,v) + S_0^2 \delta V_{\rm a}^2(u,v)/2}. \quad (32)$$

The summation is over the u, v points with $b > 3r_{\rm diff}$, which number $n_{>3} = 105$. The numerator is the squared modulus of the difference between the observed complex correlation $S_{\rm obs}(u, v)$ and the model correlation $S_{\rm calc}(u, v)$ from equation (31), with the real and imaginary parts written separately. In the denominator, $\sigma^2_{\rm m}(u, v)$ represents the variance due to measurement noise on each of the real and imaginary parts of the correlation. The second term is the corresponding variance due to random image granulation, as defined in equation (28); this term is divided by two because the definition of $\delta V_{\rm a}(b)$ in equation (28) refers to the variance of the full complex visibility, whereas in the summation in equation (32) we consider separately the signal in the real and imaginary parts of $S(u, v)$. The entire sum in equation (32) is divided by $2n_{>3}$, the number of independent fluctuations ($n_{>3}$ real and $n_{>3}$ imaginary parts) in the sum, to obtain a suitably normalized reduced χ^2.

In the right-hand side of equation (32), $S_{\rm obs}(u, v)$ and $\sigma^2_{\rm m}(u, v)$ are independent of β and $r_{\rm in}$, and $S_{\rm calc}$ is practically independent of $r_{\rm in}$ since its value is extremely small for long baselines. Therefore the entire dependence of $\chi^2_{\rm red}$ on β and $r_{\rm in}$ comes from $\delta V^2_{\rm a}(u, v)$ in the denominator. As we discussed in Section 4.1.4, this quantity does vary strongly with both parameters (see Fig. 7). Our technique is to adjust the parameters until $\chi^2_{\rm red}$ becomes equal to unity to within the appropriate tolerance. As is obvious from equation (32), such an approach is likely to be meaningful only if $\sigma^2_{\rm m}$ is smaller than, or at worst comparable with, the second term in the denominator of equation (32). This is the reason why we retained only the Lovell baselines for these calculations.

We have done two separate calculations using the long-baseline data. As we showed in Fig. 7, for any given choice of β, the excess power in the visibilities on these baselines is least when the inner scale is taken to be much smaller than $r_{\rm diff}$. Further, the power increases with increasing β. It is therefore possible to obtain an upper limit on β by choosing a very small value of $r_{\rm in}$ and then comparing the model predictions with the observations. Fig. 12(a) shows the results for Cyg X-3, where we have plotted the reduced χ^2 defined by equation (32) versus β. For low values of β, the reduced χ^2 is greater than unity, which means that the data have more fluctuations than predicted by the theory. As β increases, the discrepancy decreases such that $\chi^2 = 1$ at $\beta = 3.817$. This then is an upper bound on β, except that we have to allow a little extra latitude to take account of statistical fluctuations in the data.

Since we have 210 data points contributing to the reduced χ^2 (105 real and imaginary components), a naive estimate of the uncertainty in the reduced χ^2 is $\sqrt{2/210} = 0.098$. However, the data are not likely to be uncorrelated, because the excess power that arises from image granulation has a correlated structure in the u–v plane (GN89). We therefore employ an experimental approach to estimating the uncertainty, by looking separately at the real and imaginary parts of the visibility. We define the χ^2 of these two subsets in a straightforward fashion, as in equation (32), but retaining only the real or imaginary parts in the numerator and therefore replacing $2n_{>3}$ by $n_{>3}$ in the normalization factor. The curves of $\chi^2_{\rm red}$ for the two sets are plotted in Fig. 12(a), and each curve gives an independent upper limit for β. From this comparison we estimate that the uncertainty in the reduced

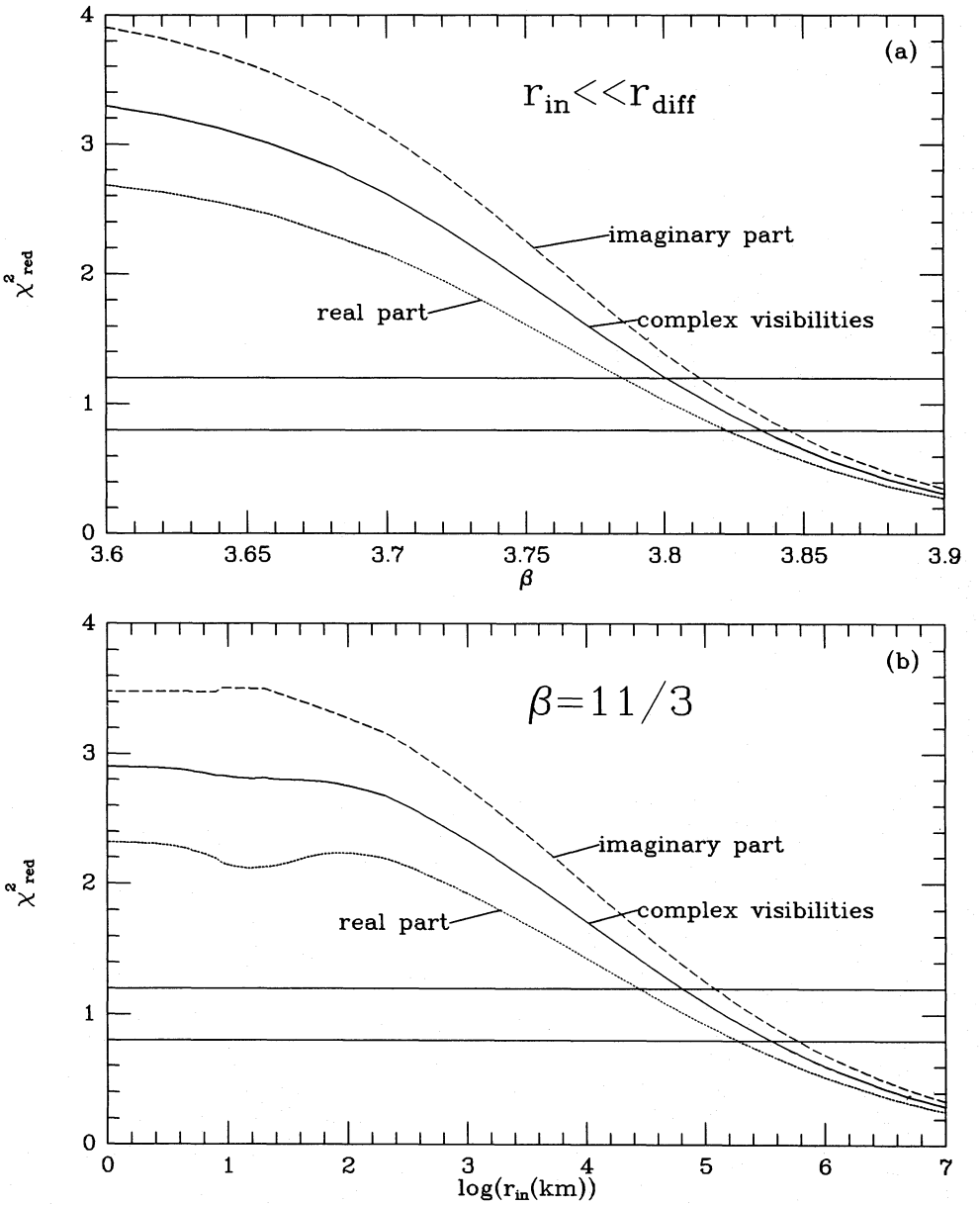

Figure 12. Results of modelling the observed visibility fluctuations in the 408-MHz data on long baselines, $b \geq 3r_{diff}$. (a) The solid line shows the variation of χ^2 with β assuming a small inner scale. The χ^2 is computed by comparing the observed visibility fluctuations with the expected variations due to measurement noise as well as Average Image granulation (Fig. 7a). Values of β that give χ^2 values lying between the two horizontal lines are acceptable. We derive an upper bound on β of 3.83 from this analysis. The dotted and dashed lines show the corresponding results when only the real and imaginary parts of the visibilities are used in the comparison. (b) Similar analysis when β is held fixed at the Kolmogorov value of 11/3 and r_{in} is allowed to be varied. We estimate $r_{in} \sim 10^{5 \pm 0.5}$ km.

χ^2 with the full data set is $\sim \pm 0.2$, and therefore that our best estimate of an upper bound on β is 3.83, which is consistent with the preliminary result given by Wilkinson et al. (1988). We can certainly rule out $\beta \geq 4$ with great confidence, and therefore this provides one more piece of evidence in favour of a shallow density-fluctuation spectrum in the ISM.

Having confirmed that we do have a shallow spectrum, in the further analysis we assumed a Kolmogorov spectrum and set $\beta = 11/3$. We could then use the same data to derive an estimate of the inner scale of the density spectrum. Fig. 12(b) shows the variation of χ^2_{red} with r_{in} for a wide range of inner scales extending from $r_{in} = 1$ to 10^7 km. The curve behaves as expected. For small values of r_{in}, the predicted image granulation due to average image effects is small, and therefore χ^2_{red} is greater than unity. As r_{in} increases, particularly once it crosses r_{diff} at $\sim 10^1$ km, δV_a^2 begins to increase and χ^2_{red} falls. χ^2_{red} crosses unity at $r_{in} \sim 10^5$ km, and continues to fall to rather small values by the right-hand edge of the plot at $r_{in} = 10^7$ km.

If the only sources of fluctuations in the visibilities are measurement noise and average image granulation as

described by GN89, then we expect χ^2_{red} to be equal to unity at the correct value of r_{in}. We therefore obtain as our best estimate, $r_{in} \sim 10^5$ km, but what is the uncertainty in this estimate?

As with the previous calculation, where we obtain an upper limit for β, we estimate the uncertainty in r_{in} by breaking up the data into subsets and looking at the variations in the predictions of each independent subset. We have done this in two ways. First, we have looked separately at the reduced χ^2 values of the real and imaginary parts of the visibility. As before, this indicates a range of uncertainty in χ^2_{red} of $0.8 \lesssim \chi^2_{red} \lesssim 1.2$, which corresponds to $10^{4.5} < r_{in} < 10^{5.5}$ km. In another approach, we divided the data into four subsets according to the value of b/r_{diff}: the first set corresponds to data with $3.0 < b/r_{diff} \leq 4.0$, the next to $4.0 < b/r_{diff} \leq 5.0$, the third set to $5.0 < b/r_{diff} \leq 6.0$, and the last set to $b/r_{diff} > 6.0$. The results were all consistent with $r_{in} \sim 10^5$ km to within an order of magnitude. Our data therefore suggest that $r_{in} \sim 10^{5 \pm 0.5}$ km. However, we are concerned that there could be additional effects at work which may affect the degree of fluctuation in the data. We therefore assess the uncertainty in r_{in} more cautiously.

Can r_{in} be much greater than $10^{5.5}$ km? We think we can rule this possibility out quite firmly. The predicted fluctuations due to image granulation increase rapidly with increasing r_{in} (Fig. 7b), and it is hard to think of any effect that could suppress this granulation and give us smaller fluctuations in the data than the theory predicts. There are only two possibilities. One is that the intrinsic size of the source may be so large as to smooth out the average image substructure in the scattered image. However, this requires an intrinsic source sized as large as a few arcsec, and this we can rule out with great confidence (see Section 3). The other possibility is that $\beta < 11/3$, but $\beta = 11/3$ has strong theoretical support from Kolmogorov turbulence theory, and in any case most observations suggest a spectrum steeper than Kolmogorov (e.g. Narayan 1988) rather than shallower.

Can r_{in} be much less than $10^{4.5}$ km? Unfortunately, the answer is yes. When we try small values of r_{in}, we find that the observed fluctuations in the visibilities are larger than the level predicted by GN89, i.e. χ^2_{red} becomes of the order of a few. This may merely mean that there *is* some additional source of fluctuating power other than the effects we have modelled. We are certain that measurement (i.e. thermal) noise cannot produce the excess fluctuations, but spurious fluctuations may arise from low-level imperfections in the interferometer data (which are hard to calibrate out at this level). We also worry about the effect of image anisotropy, which has not been taken into account in the GN89 theory. We believe we have allowed for the dominant effect of anisotropy by using the anisotropic model (29) for $r_{diff}(\theta)$, but there may be additional subtle effects, particularly since we think that the outer scale is smaller than the projected size of the image ($r_{out} < r_{ref}$). For these reasons, we prefer to be conservative and merely state that the analysis presented in this subsection constrains r_{in} to lie anywhere between 0 and $\sim 10^{5.5}$ km.

Finally, we must mention that there is clear evidence for image granularity even at 1692 MHz, e.g. the low-level mottled structure in the subtracted image shown in Fig. 6. Unfortunately, the visibilities do not extend to long enough baselines to permit the type of analysis we carried out on the 408-MHz data. If data of this quality could be collected out to twice the baseline length of our observations, say to $b \sim 500$ km, then we anticipate that we could obtain even tighter constraints on the inner scale of the turbulence.

4.3 Summary of the results on r_{in} and the prospect of better constraints

We took a model for the structure function of the form given in equation (11) corresponding to an inner scale r_{in}, and set $\alpha = 5/3$ as appropriate for a Kolmogorov spectrum of turbulence. We then used three different methods to estimate the inner scale of turbulence towards Cyg X-3: (i) from the wavelength dependence of scatter-broadening; (ii) from the visibility as a function of baseline on scales $\lesssim r_{diff}$; and (iii) from the excess fluctuations in the visibility on baselines $\gg r_{diff}$.

Method (i), which just uses a single parameter θ_{mean} derived from the observations at each wavelength, did not produce very stringent constraints: $r_{in} > 10$ km. Method (ii), which makes more complete use of the data, produced a better lower limit: $r_{in} > 100$ km. Method (iii), which is based on the magnitude of the weak granulation in the image and makes full use of recent developments in scattering theory, provided an estimate of $r_{in} \sim 10^{5 \pm 0.5}$ km. Since we were concerned about the possibility that there may be systematic enhancements in the visibility fluctuations due to image anisotropy and other effects, we prefer at this time to use this method merely to set a firm upper limit $r_{in} \lesssim 10^{5.5}$ km. The inner scale of turbulence in the scattering screen in front of Cyg X-3 is therefore in the range $\sim 10^2$–$10^{5.5}$ km.

How can this range be narrowed? For method (i), better information from VLBI on the scatter-broadened image over a range of centimetric wavelengths (i.e. where r_{diff} is $\sim 10^3$ km), coupled with improved theoretical understanding of the effect of anisotropy on the scalings, is needed. The VLBI information will be difficult to obtain, since the intrinsic size of the source components is comparable with the scatter-broadening at these wavelengths. This places a great premium on observing as soon as possible after an outburst has been detected.

For improved constraints from method (ii), well-understood VLBI data for at least one centimetric wavelength are also needed. If Spangler & Gwinn (1990) are right, and the inner scale is close to 100 km, then the tell-tale reduction below 2.0 in the slope of the $\log\{-\ln[V(b)]\}$ against $\log(b)$ plot could be established with high reliability by observing at somewhat shorter wavelengths than our 0.18 m using baselines of the order of $\sim 10^3$ km in length. Note, however, that in using method (ii) we encountered systematic effects, not related to the intrinsic structure of the source, which tend to reduce the slope of the plot and hence lead to a lowering of the inferred value of r_{in}. This is despite the fact that we eliminated the longer baselines and thus avoided the systematic effect that the excess power due to image granulation could have introduced into the fit (GN89). We therefore urge workers using this, or closely related methods, to subject their data and fitting methods to careful scrutiny. Rickett (1990) has made similar cautionary statements regarding this technique.

Method (iii) is, in principle, the best diagnostic for r_{in}, but in practice there are several complications in its use. First,

the theory of visibility fluctuations needs to be extended properly to include the effects of image anisotropy. Secondly, the interferometer data need to be particularly well understood on baselines $b \gg r_{\rm diff}$, since one will always be dealing with data in which the correlated flux density is $\lesssim 1$ per cent of the total flux density. Sources of visibility fluctuations other than thermal noise therefore need to be minimized. Obtaining better data on which to apply method (iii) demands high-SNR measurements at *decimetric* wavelengths, where the scattering is large and hence data on scales $\gg r_{\rm diff}$ are available. Much-improved MERLIN observations at 0.73 m can be obtained compared with those presented in this paper. A complete 24-h track, coupled with the inclusion of baselines to Cambridge, will greatly enhance the u, v coverage and roughly double the maximum value of $b/r_{\rm diff}$ explored. The thermal noise level on the Jodrell–Cambridge baseline (involving the Lovell telescope and the new 32-m telescope at Cambridge) will also be significantly lower than for any of the baselines in our 1986 data. At 0.18 m, longer baselines than those in MERLIN are needed to resolve the scattering disc in detail. The European VLBI Network and the VLBA will therefore be ideal instruments for studying future outbursts of Cyg X-3 at L band.

5 COMPARISON WITH OBSERVATIONS OF OTHER HIGHLY SCATTERED SOURCES

5.1 Anisotropic scattering

Our results on the anisotropic scattering of Cyg X-3 begin to form a pattern when taken with those for the few other well-studied, highly scattered sources, although there are exceptions to the trends. Thus Cyg X-3 is the third source for which the scattering disc has been shown to be markedly elliptical at at least one wavelength, the others being the Galactic Centre (Lo et al. 1993) and 2013 + 370 (Spangler & Cordes 1988a). Extremely large levels of anisotropy have also been seen in scattering by the solar wind (Narayan et al. 1989; Armstrong et al. 1990). These observations suggest that anisotropy in astrophysical scattering screens may be a widespread phenomenon, and emphasize the importance of extending GN89's theory to include the effects of anisotropy on radio wave propagation. The most highly scattered source, NGC 6334B (Moran et al. 1990), however, has a symmetric Gaussian profile at 0.2 m (FWHM ~ 2.8 arcsec) and 0.06 m (FWHM ~ 0.3 arcsec). If our explanation of the varying ellipticity seen in Cyg X-3 is correct, then the isotropic scattering of NGC 6334B implies that either $r_{\rm out}$ is smaller even than that for the scattering screen in front of Cyg X-3 or, more likely, that the screen in front of NGC 6334B is many $r_{\rm out}$ thick along the line of sight.

Frail, Kulkarni & Vasisht (1993) have obtained an estimate of $r_{\rm out}$ similar to ours (~ 0.01 pc) by an indirect argument where they compare the measured scattering of a radio pulsar with a limit on the emission measure of the scattering screen. Cordes (private communication) has carried out a similar comparison for other strongly scattered lines of sight, and again finds a small outer scale. Previously, most models of interstellar turbulence implicitly assumed that the outer scale of turbulence in the ISM must be on the order of hundreds of parsecs (e.g. Armstrong et al. 1981). We now find that the outer scale is much smaller, at least for a particular region of the ISM in the line of sight to Cyg X-3 which produces unusually large scattering.

Our explanation of the varying ellipticity in the scattered image of Cyg X-3 in terms of an outer scale ~ 0.01 pc can be easily tested by further radio observations. In our model, at all frequencies $\gtrsim 1$ GHz the image must have a constant axial ratio and position angle (0.76, 62°), whereas at frequencies below 1 GHz the image should become progressively rounder and the position angle should be random. Confirmation of this prediction will solidify our determination of the outer scale for this particular line of sight, and will provide valuable information for models of the energy input into the more highly scattering regions of the turbulent ISM.

5.2 The inner scale of turbulence

We determined that the profile of the scattering disc of Cyg X-3 is Gaussian from the Gaussian fall-off of visibility with baseline, i.e. $V(b) \propto \exp[-(b/r_{\rm diff})^{2.0 \pm 0.1}]$. The exponent of $b/r_{\rm diff}$ is also 2.0, to within the quoted errors, for NGC 6334B (2.01 ± 0.02, $r_{\rm diff} = 36$ km; Moran et al. 1990) and for the Galactic Centre (2.05 ± 0.15, $r_{\rm diff} \sim 230$ km; Lo et al. 1993). This suggests that all these observations were taken with baselines well within the inner scalelength of the respective scattering screens, and hence that $r_{\rm in}$ for highly scattered lines of sight is at least several hundred km. For less highly scattered sources, however, the results are not so consistent. For 2005 + 403 the exponent of $b/r_{\rm diff}$ is 1.95 ± 0.2 ($r_{\rm diff} \sim$ 1500 km; Mutel & Lestrade 1990). This is formally consistent with a Gaussian profile, but the Kolmogorov value of 1.67 is also compatible and hence $r_{\rm in} \ll 1500$ km cannot be ruled out. For 2013 + 370 the exponent is 1.79 ± 0.05 ($r_{\rm diff} \sim$ 1000 km; Spangler & Cordes 1988), suggesting that $r_{\rm in} \lesssim 1000$ km.

Using some of these results, combined with other scattering data from masers and pulsars, Spangler & Gwinn (1990) suggested that $r_{\rm in}$ lies in the range 50–200 km. Since no individual object has yet been studied well enough, they combined the somewhat heterogeneous results on different sources, making the assumption *faute de mieux* that the properties of the scattering medium are similar for different lines of sight through the Galaxy. Note that Rickett (1990) has cautioned, and we agree, that some of the slope determinations on which Spangler & Gwinn (1990) based their conclusions may be subject to systematic errors.

The possibility of estimating the inner scale using the low-level image granulation predicted by GN89 appears promising, and we have obtained some of the first results using Cyg X-3. Our analysis actually suggests an inner scale $r_{\rm in} \sim 10^{5 \pm 0.5}$ km, but in view of our concerns regarding possible systematic effects we have chosen to be more cautious and to interpret the results only as an upper limit $r_{\rm in} \lesssim 10^{5.5}$ km. Further accurate measurements will be required before it will be possible to make a stronger statement. At the moment, all that we can say is that the data on Cyg X-3 are compatible both with a larger value of $r_{\rm in} \sim 10^5$ km, as proposed by Coles et al. (1987) and others (Rickett & Lyne 1990; Gupta et al. 1993), as well as with a smaller value $\sim 10^2$ km (Spangler & Gwinn 1990), although both proposals are near the edge of what we can allow. As we have explained in Section 4.3,

further measurements may be able to constrain the range more tightly and may eliminate one or both proposals.

6 SUMMARY

Using MERLIN, we have obtained high-quality interferometer data on Cyg X-3 just after outburst, when its intrinsic angular size is small. These data are currently the best of their type and, in order to test some of the recent theoretical descriptions of the effect of scattering on interferometer data, we have subjected them to a careful analysis. We derive four main results, the first and most obvious of which was a surprise. Our main results are the following.

(i) The scatter-broadened image of Cyg X-3 is elliptical, and this ellipticity varies with observing wavelength. We think that the most likely explanation of the effect is that we are resolving the correlation scale of the magnetic field in the scattering screen, and hence that the outer scale of turbulence along this line of sight is $\sim$ few $\times 10^{11}$ km, i.e. $\sim$ 0.01 pc. This is very much less than galactic scales of the order of kiloparsecs that have been assumed in most previous studies (e.g. Armstrong et al. 1981). Further, the line-of-sight thickness of the screen must be no more than a few outer scales, i.e. no more than ~ 0.1 pc.

(ii) While the ellipticity and p.a. are wavelength-dependent, the profile of the scattering disc remains closely Gaussian on the MERLIN baselines. This implies that the inner scale of turbulence is larger than the diffraction scale $r_{\rm diff} \sim 100$ km at 1692 MHz.

(iii) Weak image granulations are detected in accordance with the predictions of GN89 for a 'shallow' (exponent $\beta < 4$) power-law spectrum of turbulence. The low level of the image granulations constrains the exponent β of the density fluctuation spectrum to be less than 3.83. This is consistent with the Kolmogorov value of 11/3, which is expected on theoretical grounds.

(iv) Setting $\beta = 11/3$, we use the image granulations strongly to constrain the inner scale of the turbulence to be $\lesssim 10^{5.5}$ km.

Detailed images of highly scattered sources measured over a wide range of wavelengths provide unique information on the ISM. Despite the quality of our data on Cyg X-3, we have been impressed by the difficulty of making quantitative statements about the form of the spectrum of density fluctuations along an individual line of sight. Nevertheless, we are sure that future multifrequency MERLIN and VLBI measurements will be able to place tighter constraints on the spectrum of density fluctuations for several highly scattered sources using the methods of analysis presented here. Cyg X-3 is one of the best targets if the observations are made as soon as possible after an outburst. We stress, however, that obtaining data of the requisite quality will always present a significant observational challenge.

ACKNOWLEDGMENTS

We thank K. Johnston and E. Waltman for their rapid communication of the occurrence of flares, D. Henstock for help with the data analysis, and P. Goldreich and S. Sridhar for useful discussions and comments. We are particularly grateful to J. Goodman for sharing with us his unpublished computations of the mean-square visibility fluctuations in the Average Image regime. This work was supported in part by grant AST 9148279 from the U.S. National Science Foundation.

REFERENCES

Anantharamaiah K. R., Narayan R., 1988, in Cordes J. M., Rickett B. J., Backer D. C., eds, AIP Conf. Proc. 174, Radio Wave Scattering in the Interstellar Medium. AIP, New York, p. 92
Anderson B., Conway R. G., Davis R. J., Peckham R. J., Richards P. J., Spencer R. E., Wilkinson P. N., 1972, Nat. Phys. Sci., 239, 117
Armstrong J. W., Cordes J. M., Rickett B. J., 1981, Nat, 291, 561
Armstrong J. W., Coles W. A., Kojima M., Rickett B. J., 1990, ApJ, 358, 685
Blandford R., Narayan R., 1985, MNRAS, 213, 591
Cohen M. H., Cronyn W. M., 1974, ApJ, 192, 193
Coles W. A., Frehlich R. G., Rickett B. J., Codona J. L., 1987, ApJ, 315, 666
Cordes J. M., Weisberg J. M., Boriakoff V., 1985, ApJ, 288, 221
Cornwell T. J., Wilkinson P. N., 1981, MNRAS, 196, 1067
Cornwell T. J., Anantharamaiah K. R., Narayan R., 1989, J. Opt. Soc. Am., 6, 977
Davies R. D., Walsh D., Booth R. S., 1976, MNRAS, 177, 319
Dickey J. M., 1983, ApJ, 273, L71
Fey A. L., Spangler S. R., Mutel R. L., 1989, ApJ, 337, 730
Fey A. L., Spangler S. R., Cordes J. M., 1991, ApJ, 372, 132
Frail D., Kulkarni S. R., Vasisht G., 1993, Nat, 365, 136
Goldreich P., Sridhar S., 1994, ApJ, in press
Goodman J., Narayan R., 1985, MNRAS, 214, 519
Goodman J., Narayan R., 1989, MNRAS, 238, 995 (GN89)
Gupta Y., Rickett B. J., Coles W. A., 1993, ApJ, 403, 183
Gwinn C. R., Moran J. M., Reid M. J., 1988a, in Cordes J. M., Rickett B. J., Backer C. D., eds, AIP Conf. Proc. 174, Radio Wave Scattering in the Interstellar Medium. AIP, New York, p. 129
Gwinn C. R., Moran J. M., Reid M. J., Schneps M. H., 1988b, ApJ, 330, 817
Gwinn C. R., Cordes J. M., Bartel N. H., Wolszczan A., Mutel R., 1988c, ApJ, 334, L16
Gwinn C. R., Bartel N., Cordes J. M., 1993, ApJ, 410, 673
Hewish A., 1980, MNRAS, 192, 799
Hewish A., 1992, Phil. Trans. R. Soc. Lond. A, 341, 172
Hewish A., Wolszczan A., Graham D. A., 1985, MNRAS, 213, 167
Higdon J. C., 1984, ApJ, 285, 109
Higdon J. C., 1986, ApJ, 309, 1342
Hjellming R. M., 1989, in Verschuur G. L., Kellermann K. I., eds, Galactic and Extragalactic Radio Astronomy, 2nd edn, Springer-Verlag, Berlin, p. 381
Lee L. C., Jokipii J. R., 1986, ApJ, 206, 735
Lo K. Y., Backer D. C., Kellermann K. I., Reid M., Zhao J. H., Goss W. M., Moran J. M., 1993, Nat, 362, 38
Lovelace R. V. E., 1970, PhD thesis, Univ. Cornell
Molnar L. A., Reid M. J., Grindlay J. E., 1988, ApJ, 331, 494
Moran J. M., Rodriguez L. F., Greene B., Backer D. C., 1990, ApJ, 348, 147
Mutel R. L., Lestrade J.-F., 1990, ApJ, 349, L47
Narayan R., 1988, in Cordes J. M., Rickett B. J., Backer D. C., eds, AIP Conf. Proc. 174, Radio Wave Scattering in the Interstellar Medium. AIP, New York, p. 17
Narayan R., 1992, Phil. Trans. R. Soc. Lond. A, 341, 151
Narayan R., Goodman J., 1989, MNRAS, 238, 963

Narayan R., Hubbard W. B., 1988, ApJ, 325, 503
Narayan R., Anantharamaiah K. R., Cornwell T. J., 1989, MNRAS, 241, 403
Nelson R. F., 1989, PhD thesis, Univ. Manchester
Pearson T. J., 1991, BAAS, 23, 991
Rickett B. J., 1977, ARA&A, 15, 479
Rickett B. J., 1990, ARA&A, 28, 561
Rickett B. J., Lyne A. G., 1990, MNRAS, 244, 68
Roberts J. A., Ables J. G., 1982, MNRAS, 201, 1119
Romani R. W., Narayan R., Blandford R. D., 1986, MNRAS, 220, 19
Schalinski C. J., Witzel A., Johnston K. J., Pavelin P. E., Spencer R. E., Davis R. J., Umana G., 1993, in Davis R. J., Booth R. S., eds, Sub-arcsecond Radio Astronomy. Cambridge Univ. Press, Cambridge, p. 22
Schalinski C. J., Johnston K. J., Witzel A., Spencer R. E., Fiedler R., Waltman E., Pooley G. G., Hjellming R. M., Molnar L. A., 1994, ApJ, in press
Spangler S. R., Cordes J. M., 1988, ApJ, 332, 346
Spangler S. R., Gwinn C. R., 1990, ApJ, 353, L29
Spencer R. E., Swinney R. W., Johnston K. J., Hjellming R. M., 1986, ApJ, 309, 694
Strom R. G., van Paradijs J., van der Klis M., 1989, Nat, 337, 234
Tatarskii V. I., Zavorotnyi V. U., 1980, Prog. Optics, XVIII, 204
Thomasson P., 1986, QJRAS, 27, 413
Wilkinson P. N., Spencer R. E., Nelson R. F., 1988, in Reid M. J., Moran J. M., eds, Proc. IAU Symp. 129, The Impact of VLBI on Astrophysics and Geophysics. Kluwer, Dordrecht, p. 305